



HAL
open science

Exploring the universe from deep underground to deep seas and high altitudes

Heide Costantini

► **To cite this version:**

Heide Costantini. Exploring the universe from deep underground to deep seas and high altitudes. Astrophysics [astro-ph]. Aix-Marseille Université, 2019. tel-03679081

HAL Id: tel-03679081

<https://hal.science/tel-03679081>

Submitted on 25 May 2022

HAL is a multi-disciplinary open access archive for the deposit and dissemination of scientific research documents, whether they are published or not. The documents may come from teaching and research institutions in France or abroad, or from public or private research centers.

L'archive ouverte pluridisciplinaire **HAL**, est destinée au dépôt et à la diffusion de documents scientifiques de niveau recherche, publiés ou non, émanant des établissements d'enseignement et de recherche français ou étrangers, des laboratoires publics ou privés.

AIX-MARSEILLE UNIVERSITÉ

*Mémoire présenté en vue de l'obtention de
l'Habilitation à Diriger des Recherches*

par Heide Costantini

**Exploring the universe from deep
underground to deep seas and high altitudes**

Soutenu le 4 Juillet 2019 devant le jury composé de :

Marco Anghinolfi	DR INFN	
Cristinel Diaconu	DR CNRS	
Eric Kajfasz	DR CNRS	
Hélène Sol	DR CNRS	
Sandrine Courtin	Professeur	Rapportrice
Fabrice Piquemal	DR CNRS	Rapporteur
Pierre Taxil	Professeur	Rapporteur

Contents

1	Introduction	5
2	Nuclear Astrophysics	7
2.1	Introduction	7
2.2	Stellar evolution and nuclear reactions	7
2.2.1	Nuclear reaction rate	9
2.2.2	Hydrogen burning phase	12
2.2.3	Extrapolation of laboratory data	13
2.3	LUNA	14
2.4	${}^3\text{He}(\alpha, \gamma){}^7\text{Be}$	16
2.4.1	Experimental setup	18
2.4.2	The gas target setup	18
2.4.3	The prompt γ and activation measurement	19
2.4.4	The background reduction	20
2.4.5	Angular distribution effects and detection efficiency	20
2.4.6	Comparison between activation and prompt results	25
2.5	JINA	27
	Bibliography	28
3	Astroparticle physics: ANTARES	31
3.1	Cosmic rays, neutrinos and gammas	31
3.2	Neutrino detection	35
3.3	The ANTARES detector	37
3.4	Calibration of the detector	40
3.5	The Optical Module acceptance	42
3.5.1	Optical Module simulation	43
3.5.2	The OM detection efficiency calibration measurements	47
3.5.3	Potassium 40 decay rate in the sea	49
3.5.4	Conclusion and perspectives	51
3.6	SN neutrino detection	51
3.6.1	Introduction	51

3.6.2	Simulations	52
3.6.3	Supernova signal for coincidences between OMs	52
3.6.4	Perspectives	58
	Bibliography	58
4	Astroparticle physics: CTA	61
4.1	Gamma-Rays	61
4.1.1	Gamma-rays production in astrophysical sources	62
4.2	Attenuation and detection of Cosmic gamma-rays	65
4.3	Imaging Air Cherenkov Telescopes	67
4.4	CTA: Cherenkov Telescope Array	70
4.5	Monte Carlo simulation of GCT	71
4.6	Pevatron search with CTA	79
	Bibliography	81
5	Summary and perspectives	83
	Bibliography	86
A	Curriculum Vitae	87

Chapter 1

Introduction

My research activity is tightly related to astrophysics. Starting from diploma and PhD thesis and following postdocs and permanent positions, I always worked in experiments devoted to the understanding of the mechanisms occurring in stars from the early and quiescent evolutionary stages to the final explosive ones leading to the extreme energetic scenarios that characterize the most violent Universe such as black holes and neutron stars. During my career I have mainly participated to three experiments which I will present in the following:

- LUNA is an experiment which measures nuclear reaction rates that are occurring in stars. It is located deep underground in the Gran Sasso National Laboratory in Italy. Thanks to the low cosmic background LUNA has been able to measure cross sections at energies very close to the energy region at which they take place in stars. I have worked in LUNA from 1999 to 2010, participating to the construction of the facility and to the main reaction rate measurements. The experiment, the motivation and a major measurement performed at LUNA is presented in chapter 1
- ANTARES is a neutrino telescope located in the Mediterranean sea constructed to detect neutrinos coming from the most extreme sources in the Universe. I have joined ANTARES in 2007 and have been deeply involved in the simulation of the detector and in particular in its calibration. I also performed a feasibility study to determine the sensitivity of the telescope to detect neutrinos from a supernova explosion. The experiment, the calibration activity and the sensitivity study of supernova neutrinos is presented in chapter 2.
- CTA is the next generation high energy gamma-ray observatory. I joined

CTA in 2010 and it has become my principle activity since 2014. I have been mainly involved in the simulation of the telescopes and recently in the sensitivity studies for the detection of PeV galactic cosmic rays sources known as PeVatrons. The CTA observatory, together with simulation of the telescopes and the work on the search for PeVatron sources is presented in chapter 3.

In chapter 4 I summarize the scientific challenges I have faced during my research career in the context of the past and present scientific panorama and I present the perspectives for the next years. In Appendix A an extended Curriculum Vitae is presented.

Chapter 2

Nuclear Astrophysics

2.1 Introduction

Nuclear physics plays a special role in the cosmos. Nuclear physics governs the evolution of stars from birth to their final fate. Nuclear reactions that occurred in the past in the Big Bang, in stars and in stellar explosions have created every single chemical element found in nature today (with the exception of hydrogen). The theories of nucleosynthesis have identified the most important sites of element formation and also the diverse nuclear processes involved in their production. The detailed understanding of the origin of the chemical elements combines astrophysics and nuclear physics, and forms what is called nuclear astrophysics. Nuclear fusion reactions are at the heart of nuclear astrophysics. They influence sensitively the nucleosynthesis of the elements in the earliest stages of the universe and in all the objects formed thereafter, and control the associated energy generation, neutrino luminosity, and evolution of stars. Nuclear astrophysics has come a long way since its beginnings in the early 20th century, largely coinciding with the birth of nuclear physics. Despite of this long history there have been and still are surprisingly large number of broad and fundamental open questions going from Big Bang nucleosynthesis, Solar composition, late stellar evolutionary stages, SuperNova explosions.

2.2 Stellar evolution and nuclear reactions

A star like our Sun is born from an interstellar cloud by gravitational contraction on a time scale typically of 10 million years. However, this gravitational collapse stops after this time and the star reaches a stable situation. The reason is the following. Consider the surface layer of the Sun with a temperature of 5800 K. This layer presses with its weight on the next lower layer,

which must have thus a higher temperature in order that its heat pressure can balance the overlying weight. But the surface layer and this second layer press even more on the next deeper layer, which then must have a still higher temperature. If one continues this consideration to deeper and deeper layers, one eventually reaches the centre of the Sun, for which the astrophysicists have calculated a temperature of 15×10^6 K. This high temperature must be sustained by an energy source, which is derived from the H-burning process: $4^1\text{H} \rightarrow ^4\text{He} + 2e^+ + 2\nu$ with an energy release of 26 MeV per process. In order to win the battle against the ever pressing gravitational force, the Sun must consume about 700 million tons of hydrogen in every second. Taking into account the mass of the Sun and the fact that only 10% of the central solar mass can reach the needed high temperature, the lifetime τ of the Sun with its present luminosity L (the energy radiated into space per unit of time) is about 10 billion years. This is consistent with the observations of geology and palaeontology. More massive stars than the Sun must spend even more hydrogen in the battle: one finds a proportionality $L \sim M^4$, where M is the stellar mass. Due to the larger luminosity, massive stars have a higher surface temperature than the Sun and also their lifetime is significantly shorter than that of the Sun, scaling roughly as $\tau \sim 1/M^2$. For example, a star with a 20 fold higher mass than the Sun will live only for about 25 million years. A star at this stage of evolution, i.e. H-burning, is called a main-sequence star. When a star has consumed its hydrogen in the core, the central material is replaced by the ashes ^4He of the H-burning. These ashes can again gravitationally contract until the core reaches a sufficiently high temperature, higher than in the H-burning, so that helium burning can proceed: $3\ ^4\text{He} \rightarrow ^{12}\text{C}$ and $^{12}\text{C}(\alpha, \gamma)^{16}\text{O}$ with an energy release of about 8 MeV per reaction. In this way, a star is again stabilized winning its second battle against gravity. Due to the smaller energy release, this He-burning phase has a shorter lifetime than that of H-burning. As a result of the He-burning carbon and oxygen are produced in the innermost region of the star. After the central He exhaustion, the stellar CO core contracts and the core temperature rises. Only stars with masses greater than 10 solar mass develop temperatures large enough for further nuclear burning phases. The game between pressing and heating continues for these stars with C-burning, O-burning, Ne-burning and Si-melting [1], whereby a star eventually produces elements up to the Fe region. At this stage, the nuclear matter has reached its highest binding energy per nucleon and consequently no further nuclear energy source is available. Now, gravity wins the battle and the star collapses. If the core of the star has at this stage a mass less than 1.5 solar mass, the gravitational collapse is stopped only by the electrons via the Pauli principle and the star becomes a white dwarf, of the size of the Earth.

If the mass is below 2.5 solar mass the star becomes a neutron star, with a typical size of 20 km again stabilized by the Pauli principle of the neutrons. Moreover, when the core reaches the nuclear density a rebound occurs leading to an outward moving shock wave; this is a so-called type II supernova explosion. If the mass is higher than 2.5 solar mass it becomes a black hole. In low and intermediate mass stars, the development of a high pressure from electron degeneracy and the cooling caused by the production of neutrinos prevent the onset of the C-burning. These stars conclude their life as CO white dwarfs. In the case of a close binary system such a CO white dwarf might accrete mass from its companion and thus explode as a nova or a type Ia supernova. In all the cases the star ejects in the evolution its outer envelope into space, e.g. as a ring nebula or as an explosive debris, such as in supernova.

2.2.1 Nuclear reaction rate

In an astrophysical plasma the constituent nuclei are usually in thermal equilibrium at some local temperature T . Occasionally, they collide with other nuclei, whereby two different nuclei can emerge from the collision, $1 + 2 \rightarrow 3 + 4$. The nuclei 1 and 2 form the entrance channel of the reaction and the nuclei 3 and 4, the ejectiles, form the exit channel of the reaction. If the nuclear reaction Q-value, $Q = (m_1 + m_2 - m_3 - m_4)c^2$ (m_i = nuclear masses, c = velocity of light), is positive, there is a net production of energy in the reaction for each event. Such reactions are most important for the energy generation in stars. Of equal importance is the intrinsic probability that a given reaction will take place. This probability, expressed as an energy-dependent cross section $\sigma(E)$, determines how many reactions occur per unit time and unit volume. Hence, together with the Q-value, $\sigma(E)$ provides important information on nuclear energy generation in stars. The cross section $\sigma(E)$ of a nuclear fusion reaction is of course governed by the laws of quantum mechanics where, in most cases, the Coulomb and centrifugal barriers arising from nuclear charges and angular momenta in the entrance channel strongly inhibit the penetration of one nucleus into another. This barrier penetration leads to a steep energy dependence of the cross section. Other energy-dependent effects, such as resonances and their mutual interference effects, also play important roles and the energy dependence of $\sigma(E)$ can be quite complex. In the hot stellar matter the energies of the moving nuclei can usually be described by a Maxwell Boltzmann distribution, $\sigma(E) \propto E e^{(E/kT)}$, where k is the Boltzmann constant. Folding the cross section with this energy (or velocity) distribution leads to the nuclear reaction rate per pair of nuclei [1]:

$$\langle \sigma v \rangle = (8/\pi\mu)^{1/2} (kT)^{3/2} \int_0^\infty \sigma(E) e^{(E/kT)} dE, \quad (2.1)$$

where v is the relative velocity of the pair of nuclei, E is the centre-of-mass energy and $\mu = m_1 m_2 / (m_1 + m_2)$ is the reduced mass of the entrance channel. In order to cover the different evolutionary phases of stars, i.e. from main-sequence stars such as our Sun ($T \approx 10^7$ K) to SN or the big bang ($T \approx 10^9$ K), one must know the reaction rates over a wide range of temperatures, which in turn requires the availability of $\sigma(E)$ data over a wide range of energies. For the important class of charged-particle-induced fusion reactions, there is a repulsive Coulomb barrier in the entrance channel of height $E_c = Z_1 Z_2 e^2 / r$, where Z_1 and Z_2 are the integral nuclear charges of the interacting particles, e is the unit of electric charge and r is the radius. Due to the tunnelling effect through the Coulomb barrier, the cross section drops nearly exponentially with decreasing energy (figure 2.1):

$$\sigma(E) = S(E)E^{-1} \exp(-2\pi\eta), \quad (2.2)$$

$\eta = 2\pi Z_1 Z_2 e^2 / h\nu$ is the Sommerfeld parameter ($h =$ Planck constant). The function $S(E)$, defined by this equation, contains all nuclear effects and is referred to as the nuclear or astrophysical $S(E)$ factor. If equation (2.2) is inserted in equation (2.1), one obtains

$$\langle \sigma v \rangle = (8/\pi\mu)^{1/2} (kT)^{3/2} \int_0^\infty S(E) \exp(-E/kT - b/E^{1/2}) dE, \quad (2.3)$$

with $b = 2(2\mu)^{1/2} \pi 2e^2 Z_1 Z_2 / h$. Since for non-resonant reactions the $S(E)$ factor varies slowly with energy (figure 2.1), the steep energy dependence of the integrand in equation (2.3) is governed primarily by the exponential term, which is characterized by a peak at an energy E_0 that is usually much larger than kT , the mean thermal energy in the stellar plasma. The peak is referred to as the Gamow peak (figure 2.1); for a constant $S(E)$ value over the energy region of the peak, one finds $E_0 = (bkT/2)^{2/3}$, the Gamow energy. This is the effective mean energy for a given reaction at a given temperature. Approximating the peak by a Gaussian function, one finds an effective width $\Delta = 4(E_0 kT)^{1/2} / 3^{1/2}$. Thus, nuclear burning takes place predominantly over the energy window $E_0 \pm \Delta/2$, the thermonuclear energy range, for which information on the cross section $\sigma(E)$ must be obtained. Due to the high sensitivity of the reaction rate on the height of the Coulomb barrier, there are very distinct burning phases such as H-, He- and C-burning. Even if a star has available equal amounts of H, He and C materials, the star burns first H, while the burning of He and C is completely negligible at this stage.

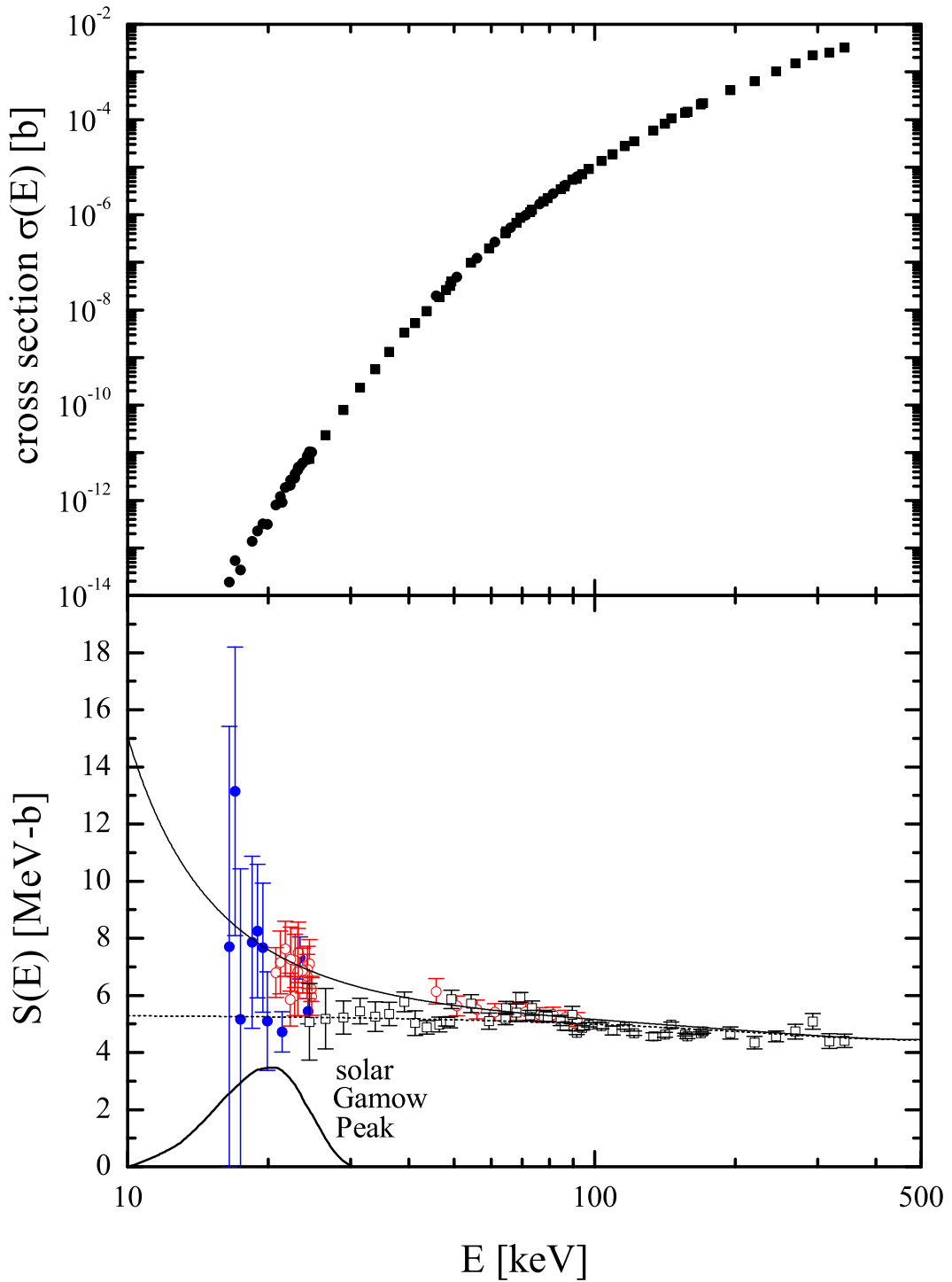


Figure 2.1: Energy dependence of the cross section $\sigma(E)$ and astrophysical $S(E)$ factor for the ${}^3\text{He}({}^3\text{He}, 2p){}^4\text{He}$ reaction. The Gamow peak shown is for solar conditions. The increasing $S(E)$ factor at low energies is due to the effects of electron screening. The blue points correspond to data taken in an underground laboratory (Gran Sasso National Laboratory) while the red and black data are taken on a surface laboratory.

energy and neutrinos. Starting with the pioneering experiment by Raymond Davis in the Homestake Cavern [4], the solar neutrino flux has been measured over several decades by different experiments aimed to proof the Standard Solar Model (SSM) of H-burning in the Sun. The deficit of measured neutrino flux in respect to the predicted one by the SSM, has given rise to the famous solar neutrino problem that was finally solved by the successful experiments of SNO and Kamland [5, 6] which proved the existence of neutrino oscillations giving an explanation of the observed solar neutrino deficit. This success opened a new era of neutrino spectroscopy, in which the solar neutrino fluxes serve as a probe for details of the standard model of particle physics. Moreover with the solution of the solar neutrino problem, the measured flux of solar neutrinos has become a very useful tool to understand the physical properties of the Sun. The solar neutrino flux depends indeed on both astrophysical inputs, such as the Sun composition, temperature and opacity, and on nuclear physics inputs that are the nuclear reaction cross sections of the reactions responsible for neutrino production. In particular the ^8B neutrino flux is known with an uncertainty of 3% from results by Superkamiokande and SNO experiments [7, 5] and the ^7Be neutrino flux has been measured by Borexino [8] with a precision of 3%. The precise knowledge of the different neutrino fluxes can be therefore exploited to understand physical properties of the sun, provided that nuclear reaction cross sections are known with similar accuracy.

2.2.3 Extrapolation of laboratory data

Due to the steep drop of the fusion cross section at subCoulomb energies, it becomes increasingly difficult to measure $\sigma(E)$ as E is lowered. Cross sections at the Gamow peak energy are of the order of 10^{-9} - 10^{-12} barn corresponding to experimental counting rate ranging from few events per day to few events per month with typical laboratory conditions. The main problem in performing these reaction measurements at surface laboratory is that the detectors are continuously bombarded by cosmic rays, that interacting with the detector, the target and the surrounding materials, create background in the detectors. The cosmic background rate is generally much larger than the reaction rate at the Gamow peak. Therefore experimentalists measure nuclear reactions at higher energies, transform the cross section into S-factor and then extrapolate the S-factor by means of different techniques (for example the R-matrix method [9]). Such an extrapolation into the unknown can lead to considerable uncertainty. At low energies there might be a change in the reaction mechanism, or in the centrifugal barrier, or there might be a contribution of narrow or subthreshold resonances to $\sigma(E)$. One effective solution to overcome the problem of cosmic background is to perform the measurements in an underground laboratory such

as the Gran Sasso National Laboratory (LNGS) in Italy, where the muon flux is reduced by several orders of magnitude. The Gran Sasso site is protected from cosmic rays by a rock cover (1400 m thick) equivalent to 3800 m water, suppressing the flux of cosmic ray induced muons by six orders of magnitude and the neutron flux by three orders of magnitude.

In figure 2.3(a) a comparison between a spectrum taken with the same Germanium detector in a surface laboratory and at LNGS, is shown. In the energy region above 3-4 MeV the gamma background is reduced approximately by three orders of magnitude. The measurement of nuclear reactions with Q-values larger than 3 MeV ($d(p, \gamma)^3\text{He}$ for the p-p chain and $^{14}\text{N}(p, \gamma)^{15}\text{O}$ for the CNO cycle for example), can therefore fruitfully benefit of an underground measurement. The spectrum region below 3 MeV is dominated by γ radiation coming from environmental radioactive isotopes (^{40}K , ^{208}Tl , ^{214}Bi etc.) and this background is not reduced in an underground environment since those isotopes are present in the rocks surrounding the laboratory. Therefore in the case of low Q-value reactions, the advantage of an underground laboratory is not evident at first sight. Detectors can be shielded passively with proper lead and copper shield as on surface. However there is a big advantage in a underground laboratory. In a surface laboratory passive shielding can be built around the detectors but above a certain thickness the shield efficiency can not be increased by adding further shield material since cosmic muons interact with the shielding material and can create background signals in the detector. Obviously this problem is dramatically reduced in an underground laboratory. Figure 2.3 (b) shows a comparison between two germanium spectra taken underground with and without a massive 0.3 m³ shield of lead and copper around the detector. The background reduction obtained underground with the passive shield is of three to four orders of magnitude.

2.3 LUNA

The first and unique accelerator facility in an underground laboratory has been LUNA. LUNA (Laboratory for Underground Nuclear Astrophysics) has been designed to measure nuclear reactions mainly of H-burning both of p-p chain and CNO cycle at energies as close as possible to the Gamow peak. It is located deep underground in the LNGS laboratory and its activity started in 1992 with the installation of a 50 KV platform with the aim to measure one of the key reactions for solar neutrino production: the $^3\text{He}(^3\text{He}, 2p)^4\text{He}$ nuclear reaction. At those times the "solar neutrino problem" was still present and a possible solution to explain the lack of detected solar neutrinos was suggested to be found in one or more of the areas of neutrino physics, solar

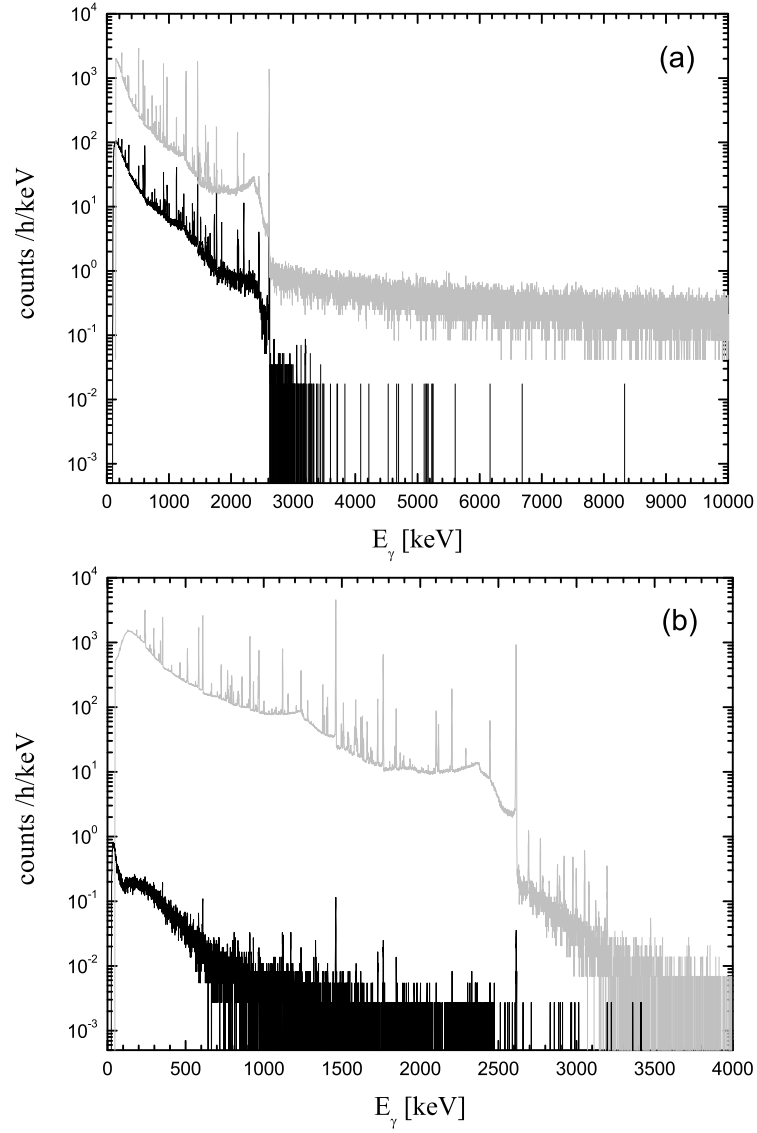


Figure 2.3: The upper panel shows the spectrum of gamma-ray background as observed with a Ge detector placed outside (grey line) and inside (black line) of LNGS. The lower panel shows a comparison of low-energy spectra inside LNGS without lead shielding (grey line) and including a heavy lead shield (black line).

physics or nuclear physics. The direct measurement at solar energies of the ${}^3\text{He}({}^3\text{He}, 2p){}^4\text{He}$ [11] reaction rate excluded a nuclear solution of the solar neutrino problem due to a resonance in this reaction channel. The studies with the first LUNA underground accelerator were concluded with a measurement of the $d(p, \gamma){}^3\text{He}$ reaction, the first case of a capture reaction studied over the full energy range of the solar Gamow peak [12, 13, 14]. The interest for a low energy measurement of this reaction was quite broad. Indeed this reaction plays an important role in the d-burning phase of proto-stars (stars in the pre-main sequence phase) and has also been a direct test of calculations based on three-body electromagnetic currents. During my PhD thesis I participated to the construction of the experimental setup, the data taking and the analysis of this nuclear reaction measurement.

After the success of this first phase a 400 kV accelerator was installed in 2000 and has been operational since then. One of the main features of an underground nuclear reaction measurement is the extremely low cross section, therefore high beam currents up to several hundreds of μA become a fundamental requirement. The 400 kV accelerator is an electrostatic machine. Helium and proton beams are operated at currents of approximately 500 μA for protons and 250 μA for α .

The first reaction measured during the second phase of LUNA has been the ${}^{14}\text{N}(p, \gamma){}^{15}\text{O}$. This reaction has been the main topic of my PhD thesis. It is the slowest reaction of the CNO cycle in hydrogen burning and therefore it directly influences the CNO neutrino flux from the Sun. Moreover it plays a key role in the determination of the age of Globular Clusters, which are among the oldest objects in the universe, determining a lower limit for the age of the universe. During my PhD I have contributed to the data-taking and data analysis of the reaction measurement [15, 16, 17, 14].

After my PhD I have continued to work in the LUNA project and in particular I have been involved in the measurement of the ${}^3\text{He}(\alpha, \gamma){}^7\text{Be}$ reaction. I have been responsible for the construction and characterization of the interaction chamber and the recycling-purification of the extended ${}^3\text{He}$ gas target. I have participated to the data-taking and contributed to the data analysis of the reaction measurement in particular for the prompt γ method analysis presented below.

2.4 ${}^3\text{He}(\alpha, \gamma){}^7\text{Be}$

The ${}^3\text{He}(\alpha, \gamma){}^7\text{Be}$ reaction has represented the largest nuclear physics uncertainty in the prediction of the flux of solar neutrinos. Since the neutrino flux of ${}^8\text{B}$ and ${}^7\text{Be}$ have been measured with an uncertainty of 3% [5, 6, 8], a similar

uncertainty on the nuclear physics inputs has been demanded in order to be able to constraint physical properties of the sun. Moreover it appeared possible to exploit neutrinos from the CNO-cycle and pp-chain to determine the primordial solar core abundances of C and N, and in general the primordial solar metallicity but the uncertainties in nuclear cross sections and neutrino oscillation parameters limited the precision and should have been reduced. The important energy range for solar physics for the ${}^3\text{He}(\alpha, \gamma){}^7\text{Be}$ reaction is $E_0 = 1$ to 4 keV.

The ${}^3\text{He}(\alpha, \gamma){}^7\text{Be}$ reaction has also important implication in Big Bang Nucleosynthesis (BBN). A comparison of the abundances of the primordial elements (D, ${}^3\text{He}$, ${}^4\text{He}$ and ${}^7\text{Li}$) from measurements of the cosmic microwave background radiation using the Wilkinson microwave Anisotropy Probe (WMAP [20]) and astronomical observations demonstrated a good agreement for the D and ${}^4\text{He}$ abundance. However, the predicted abundance of ${}^7\text{Li}$ was a factor 2 to 3 higher than observations. Nowadays this discrepancy for ${}^7\text{Li}$ is even larger after the precise microwave background measurements of the Planck satellite [21] and ${}^7\text{Li}$ predictions are now a factor of four higher than observations. According to the standard model of BBN, ${}^7\text{Li}$ is produced by the ${}^3\text{He}(\alpha, \gamma){}^7\text{Be}$ reaction followed by the electron capture of ${}^7\text{Be}$. Therefore this reaction rate is the necessary basis for possible solutions of the ${}^7\text{Li}$ problem. The important energy range of the BBN for the ${}^3\text{He}(\alpha, \gamma){}^7\text{Be}$ reaction is $E_0 = 80$ to 400 keV.

The ${}^3\text{He}(\alpha, \gamma){}^7\text{Be}$ reaction is a capture process that occurs through the formation of a ${}^7\text{Be}$ nucleus with the emission of γ -radiation coming from the direct capture into the ground state and into the first excited state of ${}^7\text{Be}$. The ${}^7\text{Be}$ decays by electron capture to the first excited state of ${}^7\text{Li}$ with a branching ratio of $10.44 \pm 0.04\%$ [22] and subsequently emits a γ of 478 keV. Before the LUNA results, the absolute cross section of the ${}^3\text{He}(\alpha, \gamma){}^7\text{Be}$ reaction was derived either from the observed flux of capture γ -rays (prompt γ method) either from the observed radioactivity of the residual nuclei ${}^7\text{Be}$, i.e. its electron capture to ${}^7\text{Li}$ with $T_{1/2} = 53$ days (activation method). An apparent discrepancy of about 9% between the results obtained from the two methods was found. The origin of it might be found either in the underestimation of systematic effects or in the presence of non-electromagnetic transition (monopole) that can explain the 9% larger value of the activation measurements with respect to the prompt γ -rays. To improve the knowledge of this reaction, LUNA decided to perform a new precision measurement using both activation and prompt γ methods at the same time to reduce systematic errors.

2.4.1 Experimental setup

The ${}^3\text{He}(\alpha,\gamma){}^7\text{Be}$ reaction cross section was studied at energies $E_\alpha=220$, 250 and 400 keV using the 400 kV LUNA2 accelerator.

2.4.2 The gas target setup

The measurement was performed using an extended windowless ${}^3\text{He}$ gas target setup. It consists in a three differential pumping stages separated by high flow impedance collimators that allow the pressure to drop from a typical value of 0.7 mbar in the target chamber to 10^{-6} mbar, that is the pressure of the accelerator tube. During the experiment the ${}^3\text{He}$ gas was recovered from the first and the second pumping stages, purified through an industrial purifier, and fed back to the target chamber.

The pressure inside the target chamber was continuously monitored during the experiment with capacitance gauges at two different positions: one close to the entrance collimator, and an other approximately at the center of the target chamber. The pressure and temperature profile inside the target chamber and in the connecting pipe between the interaction chamber and the first pumping stage have been measured with a dedicated chamber identical to the one used during the measurements, but with several apertures along the target length. From these measurements the target thickness without beam was obtained with an uncertainty of 0.8% [23]. Due to the intense α beam, the target density along the beam path was decreasing due to the well-known beam heating effect [24]. This phenomenon was investigated using a 100 μm thick silicon detector positioned inside the target chamber, detecting the projectiles elastically scattered first in the target gas and subsequently in a movable 15 $\mu\text{g}/\text{cm}^2$ carbon foil (see Figure 2.4). This effect was measured at different target gas pressures and at different positions in the target along the beam path. Details on the elastic scattering measurements are described in [25]. The purity of the target was also monitored using the elastic scattering [25] and during the whole experiment the nitrogen contamination always remained below 3%. The overall uncertainty on the target density considering the without and the with-beam density measurements and the uncertainty on the gas purity corrections, is of 1.5%.

The beam entered the interaction chamber through the 7 mm diameter collimator and was stopped on a detachable copper disk that served as the primary catcher for the produced ${}^7\text{Be}$ and as the hot side of a power calorimeter (see figure 2.4). The latter was used to measure the beam intensity from the difference between the calorimeter power values with and without beam and was similar to the one used in previous experiments of LUNA [12]. The

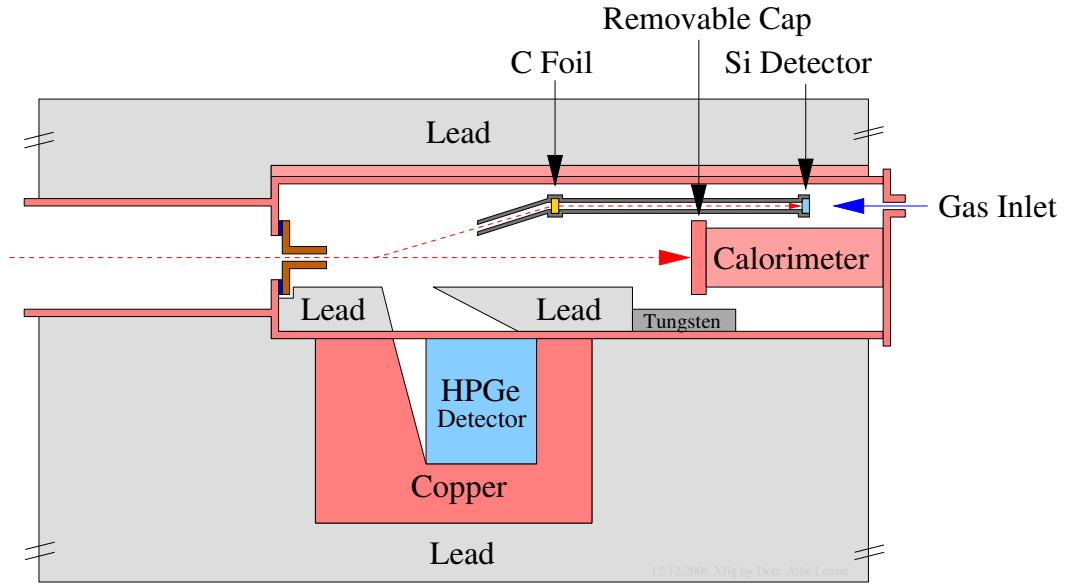


Figure 2.4: Schematic view of the interaction chamber with the position of the HPGe detector and of the $100\ \mu\text{m}$ silicon detector used for ${}^3\text{He}$ density monitoring. The distance between the entrance collimator and the calorimeter is 35 cm.

calorimeter was calibrated in the whole energy range, using the evacuated target chamber as a Faraday cup. The calibration was periodically repeated during the entire measurement. The reproducibility of the calibrations was within 1.5%: this value was adopted as the uncertainty on the beam current determination.

2.4.3 The prompt γ and activation measurement

The main feature of the LUNA measurement of the ${}^3\text{He}(\alpha, \gamma){}^4\text{He}$ reaction has been to measure the cross section by using both prompt γ and activation techniques at the same time. The prompt γ s were detected by a HpGe detector positioned at close distance to the extended ${}^3\text{He}$ gas target, while the delayed γ s coming from the decay of the ${}^7\text{Be}$ in ${}^7\text{Li}$ were detected by a HpGe detector heavily shielded in the low activity laboratory of LNGS. Indeed after each run the calorimeter cap that served as a catcher for the implanted ${}^7\text{Be}$ nuclei, was dismantled and brought to the low activity laboratory. My work has been mainly focused on the prompt γ -measurement, therefore in the following I will not enter in the details of the activation measurement. Details of this part of the experiment can be found in a dedicated paper [23].

2.4.4 The background reduction

The prompt γ rays coming from the direct capture to the first excited state and ground state of the ${}^7\text{Be}$ nucleus, were detected by a 137% (relative efficiency) HPGe detector (figure 2.4) positioned with its front face 7 cm from the beam axis. Since the energies of the prompt γ rays (0.4, 1.3 and 1.7 MeV) are in the energy region of natural radioactive isotopes, a massive 0.3 m³ copper and lead shielding was built around the detector and the target chamber. The entire shielding was enclosed in a anti-radon envelope, which is a plexiglas box flushed with N₂ gas to avoid ${}^{222}\text{Rn}$ background. Similar shielding was used for the off-line measurement (activation method). To further reduce the background on the detector, the target chamber was built with oxygen free high conductivity copper and no welding materials were used in the chamber assembly. Moreover low activity materials were used to build the silicon detector support and all the equipment inside the target chamber (figure 2.5).

In this way, a background suppression of 5 orders of magnitude was reached for γ rays below 2 MeV with respect to a background spectrum measured underground with no shielding [26]. Aside from radioactive isotopes, background could come also from beam induced reactions. A background measurement at $E_\alpha=400$ keV substituting ${}^3\text{He}$ gas with inert ${}^4\text{He}$ gas was performed but no additional counts were detected with respect to the laboratory background. Further details regarding the γ ray background can be found elsewhere [26].

2.4.5 Angular distribution effects and detection efficiency

According to radiative direct capture model calculations [27] the ${}^3\text{He}(\alpha,\gamma){}^7\text{Be}$ direct capture mainly proceeds by E1 transition that can occur through s or d waves. The angular distribution function $W(\theta)$ can be expressed as:

$$W(\theta) = 1 + a_1 P_1(\theta) + a_2 P_2(\theta) + \dots \quad (2.4)$$

where a_1 and a_2 are the coefficients of the Legendre Polynomials $P_1(\theta)$ and $P_2(\theta)$. To minimize the systematic error due to angular distribution uncertainty, a lead collimator has been inserted inside the target chamber (figure 2.4) to collect at the HPGe detector mostly the γ rays emitted around 55°, angle at which the second Legendre Polynomial vanishes.

This collimator is a lead brick, 3 cm thick, with a hole shaped as a truncated cone with elliptical base and the main axis inclined with respect to the vertical of 45° (figure 2.4). This particular shape was studied with the LUNA Monte Carlo code [28] taking into account the extended target effect and the

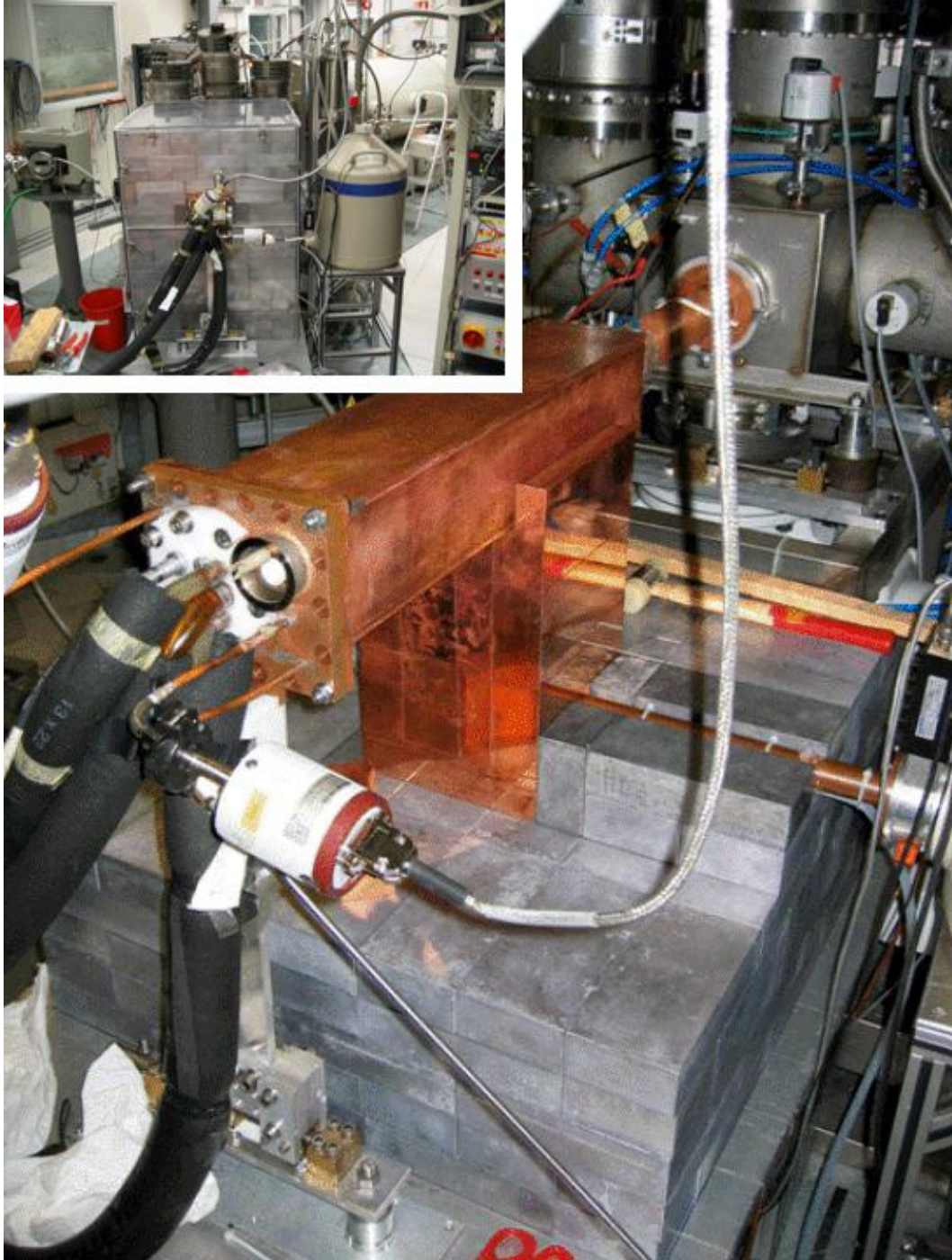


Figure 2.5: Photo of the construction phase of the lead shield for the ${}^3\text{He}(\alpha, \gamma){}^4\text{He}$ experiment. The copper enclosing the HPGe detector and the copper target chamber are visible. The inset shows the completed 0.3m^3 lead shield surrounded by a radon box.

detector solid angle, which depends on the HPGe detector dimensions and its distance from the beam. The lead collimator and a tungsten brick (1.6 cm thick) were positioned in the target chamber also to shield the detector from possible beam induced radiations coming from the calorimeter cap, and from laboratory background coming from the upstream and downstream apertures in the shielding. In an extended gas target, the interactions are taking place along the whole beam path and each interaction has a different geometrical subtending angle to the detector. The detection efficiency profile $\eta(z)$ has been measured moving a ^{60}Co ($E_\gamma=1173, 1332$ keV) and ^{137}Cs ($E_\gamma=662$ keV) point-like sources along the beam axis from the collimator to the calorimeter cap. Due to the particular shape of the inner lead collimator, the efficiency profile along the target length was quite complicated and the LUNA Monte Carlo simulation code was used to evaluate the detection efficiency for the $^3\text{He}(\alpha,\gamma)^7\text{Be}$ γ lines. The crucial point in the simulation has been the HPGe description and in particular the determination of the active volume of the detector, information not provided by the manufacturer. To determine this parameter, the inner collimator was removed from the chamber and a first set of efficiency measurements was performed using the calibrated point-like sources placed in several points along the beam path. By comparing the MC simulations with the results of these first measurements, the detector geometry was determined. Subsequently, measurements and simulations were performed with the inner lead collimator. A comparison between the simulated and the experimental efficiency profiles $\eta(z)$ is shown in figure 2.6.

The simulation reproduced the integrated experimental efficiency within the source activity uncertainties (1.5%). With the detector geometry fixed through the comparison with the ^{60}Co and ^{137}Cs sources, and the detailed description of the target geometry (i.e. inner Pb and W collimator geometry), the simulation reproduced the experimental $^3\text{He}(\alpha,\gamma)^7\text{Be}$ γ spectra at the level shown in figure 2.7. Summing effects between the primary and the secondary γ transitions in the $\text{DC}\rightarrow 429\rightarrow 0$ cascade, actually smaller than 1%, were considered in the MC simulation and included in the data analysis.

Angular distribution functions have previously been calculated down to 210 keV [27] and showed a small anisotropy for both the transition to the first excited state (γ_1) and to the ground state (γ_0). Experimental measurements carried out down to $E_{cm}=148$ keV [29] confirmed the anisotropy manifesting interference effects of both partial wave contributions. Recent theoretical predictions [30] are in agreement with the theoretical angular distribution functions of [27]. Predictions of a_1 and a_2 can be found in [27] as a function of the incident beam energy. These curves have been linearly extrapolated down to 200 keV and the coefficients of the Legendre polynomials adopted in the

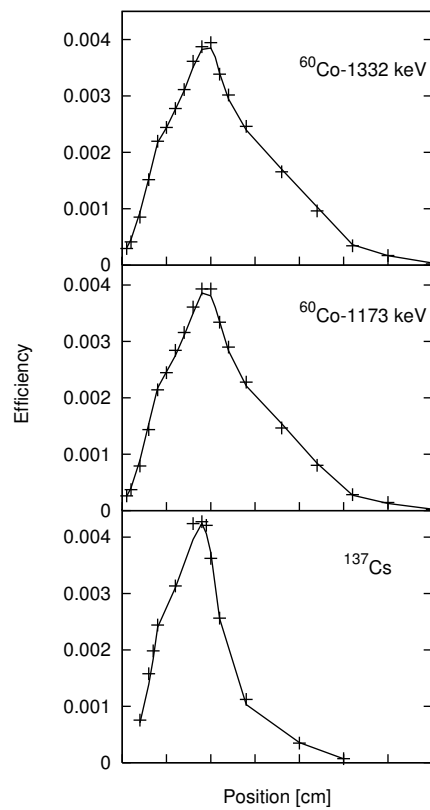


Figure 2.6: Efficiency profiles measured using point-like sources of ${}^{60}\text{Co}$ and ${}^{137}\text{Cs}$ with the inner lead and tungsten collimators in the chamber. Crosses represent the experimental data while lines are linear interpolations of MC calculations. The zero position corresponds to the entrance of the beam inside the target chamber.

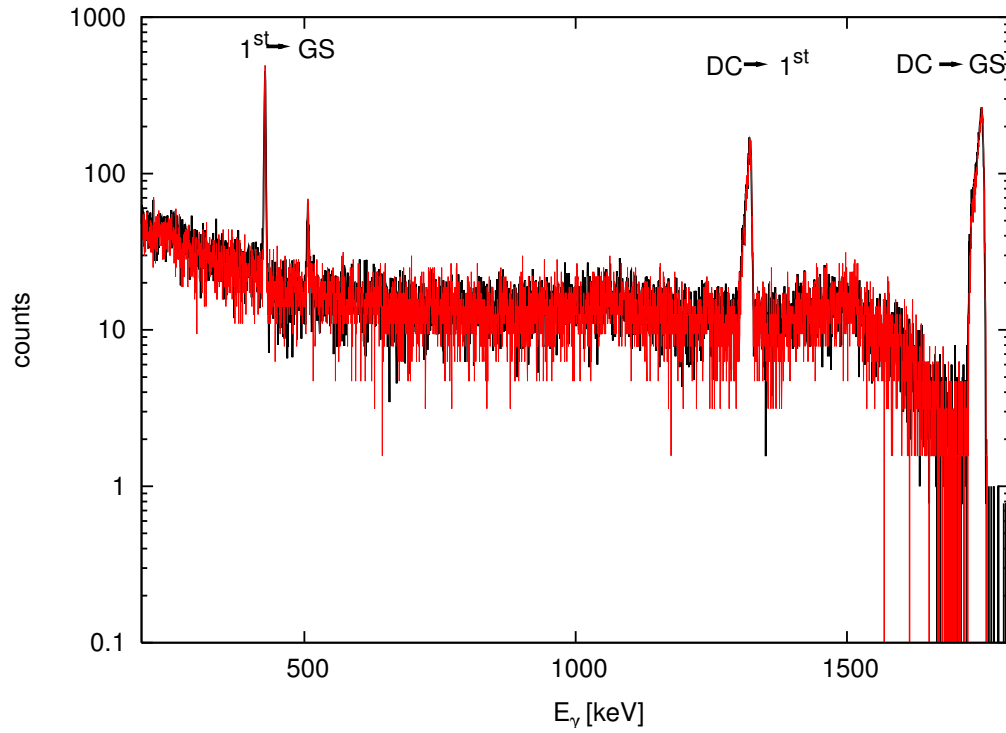


Figure 2.7: Comparison between the experimental (black curve) and the simulated (red curve) γ spectrum at $E_\alpha = 400$ keV and $P_{target} = 0.7$ mbar. The simulated spectrum was normalized to the experimental one at $E_\gamma = 1.76$ MeV to allow the shape comparison.

detection efficiency calculation are $a_1 = -0.05$ and $a_1 = 0$ for the transition to the ground and to the first excited state, respectively, and $a_2 = -0.1$ for both transitions. To estimate the effect on the detection efficiency of the uncertainty on the angular distribution, we have varied both a_1 and a_2 coefficients in the Monte Carlo simulation and 100% changes resulted in a global 2.5% variation of the detection efficiency. The latter has been assumed as a systematic uncertainty and turned out to be the major contribution to the error budget of the prompt γ experiment.

2.4.6 Comparison between activation and prompt results

A comparison between the results from the prompt γ -ray detection and activation was possible since both were carried out concurrently. After each run the calorimeter cap was dismounted and placed in front of a heavily shielded 125% HPGe detector of the low-level laboratory of Gran Sasso. This counting setup allowed to measure activities down to 25.3 ± 1.3 mBq, while a background sample irradiated with ${}^4\text{He}$ gas in the target chamber and a comparable irradiation time resulted in a background value of lower than 0.1 mBq. Since the irradiation of the samples used for off-line ${}^7\text{Be}$ counting were simultaneously performed to the γ radiation detection, some systematic uncertainties are common to both methods and were not considered in the comparison between the S factors obtained with the two techniques. In table 2.1 the sources of systematic uncertainty affecting both methods and their contribution to the final uncertainty on the S-factor, are listed.

The cross section was measured at $E = 127$ and 148 keV using activation technique only, while at $E = 93$, 106 and 170 keV the cross section was obtained using both techniques (activation and prompt γ -ray). The results from the two methods were consistent and did not show any discrepancy at the level of the achieved accuracy (4%) (see Figure 2.8). These results excluded the contribution of non-radiative contribution to the ${}^3\text{He}(\alpha, \gamma){}^7\text{Be}$ cross section, at least at these energies. No discrepancy between the two techniques was found also by a successive experiment [32] where the ${}^3\text{He}(\alpha, \gamma){}^7\text{Be}$ reaction was measured in the energy region between $E = 0.35$ and 1.2MeV . While the LUNA data covered the energy window of BBN, an extrapolation was still needed for the solar Gamow peak. An average $S(0)$ value was obtained by combining the most recent data [31, 32] at that time with the LUNA data. The combined data were fitted re-scaling two different theoretical curves (figure 2.8): a resonating-group calculation [33] and a direct capture model [34]. Following the approach indicated in [34], the final $S(0)$ value was obtained

Source	Prompt	Activation
Beam Intensity	1.5%	1.5%
^3He Target Density	1.5%	1.5%
Effective Energy	0.5-1.1%	0.5-1.1%
Angular Distribution	2.5%	
Detection Efficiency	1.5%	
^7Be counting efficiency		1.8%
Incomplete ^7Be collection		0.5%
^7Be Backscattering		0.5%
^7Be Distribution in catcher		0.4%
478 keV γ -ray branching		0.4%
^7Be Half life		0.1%
Parasitic ^7Be production		0.1%
Total	(3.6-3.9)%	(3.0-3.2)%

Table 2.1: Systematic uncertainties and their contribution to the S-factor error for the prompt and activation experiments.

from a weighted average of the extrapolated $S(0)$ for each experiment and resulted in $S(0) = 0.567 \pm 0.018 \pm 0.004$ keVb where the last error value accounts for the uncertainty of the adopted theoretical model. Thanks to those experimental results, it was possible to reduce the uncertainty on the predicted ^8B neutrino flux due to S_{34} from 7.5% to 2.4% and the total uncertainty, including astrophysical parameters, was decreased from 12% to 10%. Similarly, the uncertainty on ^7Be predicted flux was decreased from 9.4% down to 5.5%, being the contribution of S_{34} error reduced from 8% to 2.5% [35, 36]. The experimental and theoretical situation in the $^3\text{He}(\alpha, \gamma)^7\text{Be}$ reaction at $E \approx 1$ MeV has recently attracted much attention. This is so because at $E \approx 2$ MeV the modern data obtained with the European Recoil separator for Nuclear Astrophysics (ERNA) [37] were about 40% higher than the 50 years old data by Parker and Kavanagh [39]. This conclusion [37] was subsequently confirmed in a number of recent experiments. In 2014 deBoer et al. [38] performed a global R-Matrix fit (see [9] for a description of the R-matrix technique for cross section extrapolation) using $^3\text{He}(\alpha, \gamma)^7\text{Be}$ data (including the higher energy data from ERNA), as well as scattering data leading to $S(0) = 0.542 \pm 0.011(\text{MC fit}) \pm 0.006(\text{model})^{+0.019}_{-0.011}(\text{phase shift})$ keV b. This work indicated that, after the solution of the apparent discrepancy between activity and prompt γ measurements, the main uncertainty comes now from the S-factor energy dependence and it was suggested to perform a measurement of the $^3\text{He}(\alpha, \gamma)^7\text{Be}$ reaction

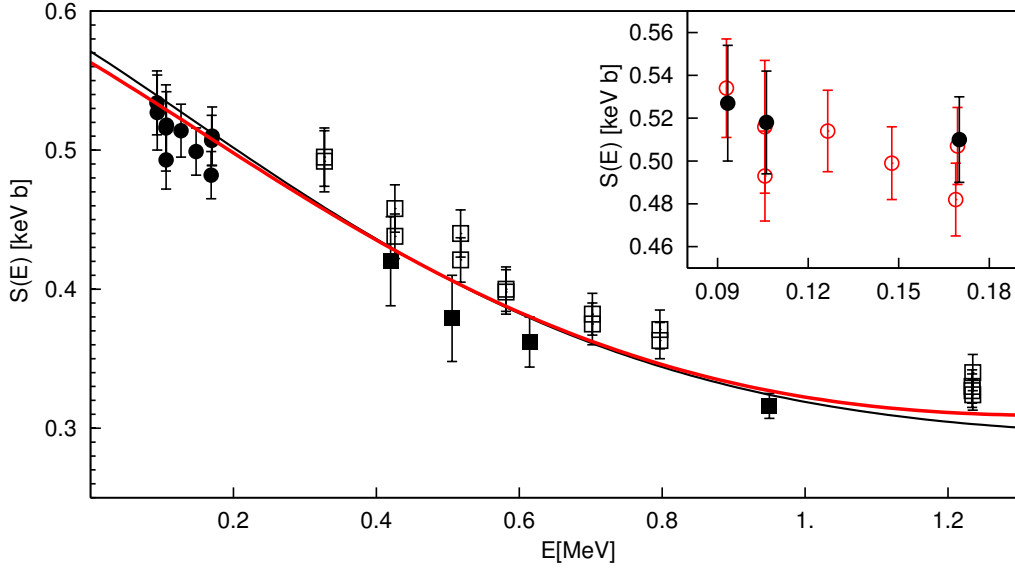


Figure 2.8: Astrophysical S factor for the ${}^3\text{He}(\alpha,\gamma){}^7\text{Be}$ reaction. The filled squares are the data from Singh et al. [31], the filled circles are the data from LUNA, and the open squares are the data from Brown et al. [32]. The thin (black) and thick (red) curves are the best fit to the data obtained re-scaling the S factor curve as described in the text from [33] and [34], respectively. The inset shows a detailed comparison of the results from the prompt γ -ray measurement (filled circles) and the activity method (open circles).

over and as wide as possible energy range using the same experimental setup. For what concerns the BBN, there is no need to extrapolate to low energies as it is needed for solar region. It can therefore be stated that the LUNA ${}^3\text{He}({}^4\text{He},\gamma){}^7\text{Be}$ data rule out any nuclear solution to the BBN ${}^7\text{Li}$ problem [40].

2.5 JINA

In 2005 I joined the JINA (Joint Institute for Nuclear Astrophysics) institute that is a joint institute of several university and national US laboratories with the aim to address open questions at the intersection of astrophysics and nuclear physics. I stayed one year as post-doctoral fellow at the Nuclear Structure Laboratory (NSL) at the University of Notre Dame (IN-USA) and continued the collaboration in the following years with several 1-month long stays. During my 1-year stay at Notre Dame I mainly focused on the measurement and analysis of the ${}^{16}\text{O}(\alpha,\gamma){}^{20}\text{Ne}$, an important reaction in stellar

He-burning phase. At quiescent He-burning temperatures, the reaction rate is considered to be low due to the lack of resonances in the relevant energy region ($E_{cm} \sim 300$ keV). This reaction is therefore considered the end-point of the main reaction chain ${}^4\text{He}(2\alpha, \gamma){}^{12}\text{C}(\alpha, \gamma){}^{16}\text{O}(\alpha, \gamma){}^{20}\text{Ne}$ and determines, together with the rate of ${}^{12}\text{C}(\alpha, \gamma){}^{16}\text{O}$, the ${}^{16}\text{O}$ abundance at the ignition of the carbon burning phase in late stellar evolution. This reaction was studied using an α -beam on a solid-target consisting of Ta_2O_5 . The emitted gammas were measured using a high-purity germanium detector. The obtained data were combined with older data from a gas target experiment performed at the Stuttgart laboratory and a global R-matrix fit was done with the aim to extrapolate the astrophysical S-factor to stellar relevant energies. Details of the measurement and analysis can be found in [41].

After my 1-year stay at NSL, a collaboration between JINA and LUNA started. In particular the ${}^{15}\text{N}(p, \gamma){}^{16}\text{O}$ nuclear reaction of the CNO cycle was studied in the full-energy range from few keV to several MeV performing the measurement both at NSL and at the LUNA accelerator [43] with very similar experimental setups. The aim of this measurement was to have compatible data sets allowing to reduce the uncertainty on the extrapolation of the astrophysical S-factor using the R-matrix technique [42]. The ${}^{15}\text{N}(p, \gamma){}^{16}\text{O}$ reaction measurement started a fruitful collaboration between the NSL and the LUNA facility with the philosophy to cover large energy regions and therefore to improve significantly the quality of final S-factor extrapolated results.

Bibliography

- [1] C. Rolfs and W. S. Rodney 1988 *Cauldrons in the Cosmos* (Chicago, IL: University of Chicago Press) (1988)
- [2] C. F. von Weizsäcker Phys. Zeitschrift 39, 663 (1938).
- [3] H.A. Bethe and C. L. Critchfield 1938 Physical Review 54, 248 (1938). 547.
- [4] R. Davis, D. S. Harmer and K. C. Hoffman Physical Review Letters 20, 1205 (1968).
- [5] Aharmin B et al, Phys. Rev. C 75 045502 (2007).
- [6] Eguchi K et al, Phys. Rev. Lett. 90 021802 (2003).
- [7] J. Hosaka et al., Phys. Rev. D 73, 112001 (2006).
- [8] G. Bellini et al. (Borexino Collaboration), Phys. Rev. Lett 107, 141302 (2011).
- [9] Lane A M and Thomas R G, Rev. Mod. Phys. 30, 257 (1958).
- [10] C. A. Barnes, K.H. Chang, T. R. Donoghue and C. Rolfs Phys. Lett. B 197, 315 (1987).

- [11] C. Arpesella et al., *Physics Letters B* 389, 452 (1996).
- [12] C. Casella et al., *Nuclear Instruments and Methods A* 489, 160 (2002).
- [13] C. Casella et al., *Nuclear Physics A* 706, 203 (2002).
- [14] H. Costantini, PhD Thesis, *Universita degli Studi di Genova* (2003).
- [15] A. Formicola et al., *Physics Letters B* 591, 61 (2004).
- [16] G. Imbriani et al., *Astronomy Astrophysics* 420, 625 (2004).
- [17] G. Imbriani et al., *European Physical Journal A* 25, 455 (2005).
- [18] A. Formicola, *Nuclear Instruments and Methods A* 507, 609 (2003).
- [19] F. Confortola, PhD Thesis, *Universita degli Studi di Genova* (2005).
- [20] R.H. Cyburt, B.D. Fields, K.A. Olive, *Phys. Lett. B* 567, 227 (2003).
- [21] Planck Collaboration, *Astronomy Astrophysics* A13, 594 (2016).
- [22] D. Tilley et al., *Nucl. Phys. A* 708, 3 (2002).
- [23] Gy. Gyurky et al., *Physical Review C* 75, 035805 (2007).
- [24] J. Grres et al., *Nucl. Instr. Meth.* 177, 295 (1980).
- [25] M. Marta et al., *Nuclear Instruments and Methods A* 569, 727 (2006).
- [26] A. Caciolli et al., *European Physical Journal A* 39, 179 (2009).
- [27] T. A. Tombrello and P. D. Parker, *Phys. Rev.* 131, 2582 (1963).
- [28] C. Arpesella et al., *Nucl. Instr. Meth. Phys. Res. A* 360, 607 (1995).
- [29] H. Krawinkel et al., *Z. Phys. A* 304, 307 (1982).
- [30] B. T. Kim, T. Izumoto, and K. Nagatani, *Phys. Rev. C* 23, 33 (1981).
- [31] B. N. Singh et al., *Phys. Rev. Lett.* 93, 262503 (2004).
- [32] T. A. D. Brown et al *Phys. Rev. C* 76, 055801 (2007).
- [33] T. Kajino, H. Toki and S.M. Austin *Astrophys. J.* 319, 531 (1987).
- [34] P. Descouvemont et al, *At. Data Nucl. Data Tables A* 88, 203 (2004).
- [35] H. Costantini et al. *Nucl. Phys. A* 814, 144 (2008).
- [36] F. Confortola et al. *Phys. Rev. C* 75m], 065803 (2007).
- [37] A. Di Leva et al., *Phys. Rev. Lett.* 102, 232502 (2009).
- [38] R.J. deBoer et al., *Phys. Rev. C* 90, 035804 (2014).
- [39] P.D. Parker, R.W. Kavanagh, *Phys. Rev.* 131, 2578 (1963).
- [40] M. Anders et al. *Phys. Rev. Lett.* 113, 042501 (2014).
- [41] H. Costantini et al. *Phys. Rev. C* 82, 035802 (2010).
- [42] R. E. Azuma et al., *Phys. Rev. C* 81, 045805 (2010).
- [43] P. J. LeBlanc et al., *Physical Review C* 82, 055804 (2010).

Chapter 3

Astroparticle physics: ANTARES

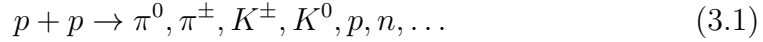
In 2006, coming back from my 1-year stay at the University of Notre Dame, I got a position as a permanent researcher at INFN (Istituto Nazionale di Fisica Nucleare) in Genova (Italy). At that time Genova was already involved in the ANTARES project: an astrophysical neutrino detector in the deep sea. The main goal of neutrino astronomy is to detect neutrinos coming from the most energetic regions of the Universe carrying complementary (if not exclusive) information about the cosmos. While my research had been mainly devoted to understand the quiescent and stable evolutionary stages of the life of a star, I started to get fascinated by the high energy sky explored in experiments such as ANTARES and I therefore joined the ANTARES collaboration in 2007. In 2010 I got a position as assistant professor at the University of Aix-Marseille (France) and started to get involved also in the CTA (Cherenkov telescope Array) project, which aims to build a large high energy gamma-ray observatory. Both ANTARES and CTA projects aim to study extreme high energy sources by means of neutrinos and gammas respectively. One of the main goals is to unveil one of the major questions in astroparticle physics namely the origin of high energy cosmic rays.

3.1 Cosmic rays, neutrinos and gammas

Cosmic rays (CRs) are high-energy nuclei (mainly protons) with a wide energy spectrum (see Figure 3.1) which spans for more than 10 orders of magnitude up to 10^{20} eV. The measured power law spectrum of CRs is characterized by the index $\alpha=2.7$ up to energies of roughly 3×10^{15} eV and $\alpha= 3.1$ in the region above. This feature in the energy spectrum is known as the knee. At 10^{19} eV,

a flattening in the spectrum is observed by most experiments, denoted as the ankle where it is generally assumed that these CRs are of extragalactic origin.

The primary mechanism by which particles gain energy beyond the thermal energy is the Fermi mechanism where the charged particle is accelerated by iterative scattering processes on a shock wave produced during exceptional events, like stellar gravitational collapses. Due to the magnetic fields confinement, the scattered particles are trapped inside the acceleration region and have a small probability to escape. The Fermi mechanism predicts a power law differential energy spectrum $\sim E^{-2}$ and fits correctly to the energy dependence involved in galactic cosmic rays. Assuming that at these acceleration sites a fraction of the high-energy CRs interact with the ambient matter or photon fields, TeV gamma-rays are produced by the π^0 decay while neutrinos are produced by charged pion decay. This is the so-called astrophysical hadronic model. These mesons are produced either by proton-proton collisions via [1]



where ...represent the presence of higher mass mesons and baryons. This process is often referred as the astrophysical beam dump mechanism. The cross section corresponds to about 40-50 mb. A second process producing secondary mesons is due to accelerated protons interacting in the surroundings of the CRs emitter with photons predominantly via the Δ^+ resonance:



This process is called photoproduction and the cross section at the resonance is of ~ 0.250 mb. Although the photoproduction cross section is two orders of magnitude smaller than the cross section of the beam dump process, in some astrophysical environments the probability that neutral and charged pions are produced by photoproduction is much higher than the probability that they are produced by beam dump. This is because the number density of ambient photons could be much larger than that of environmental matter number density.

Neutral mesons decay in photons (observed at Earth as gamma-rays):



while charged mesons decay in neutrinos:

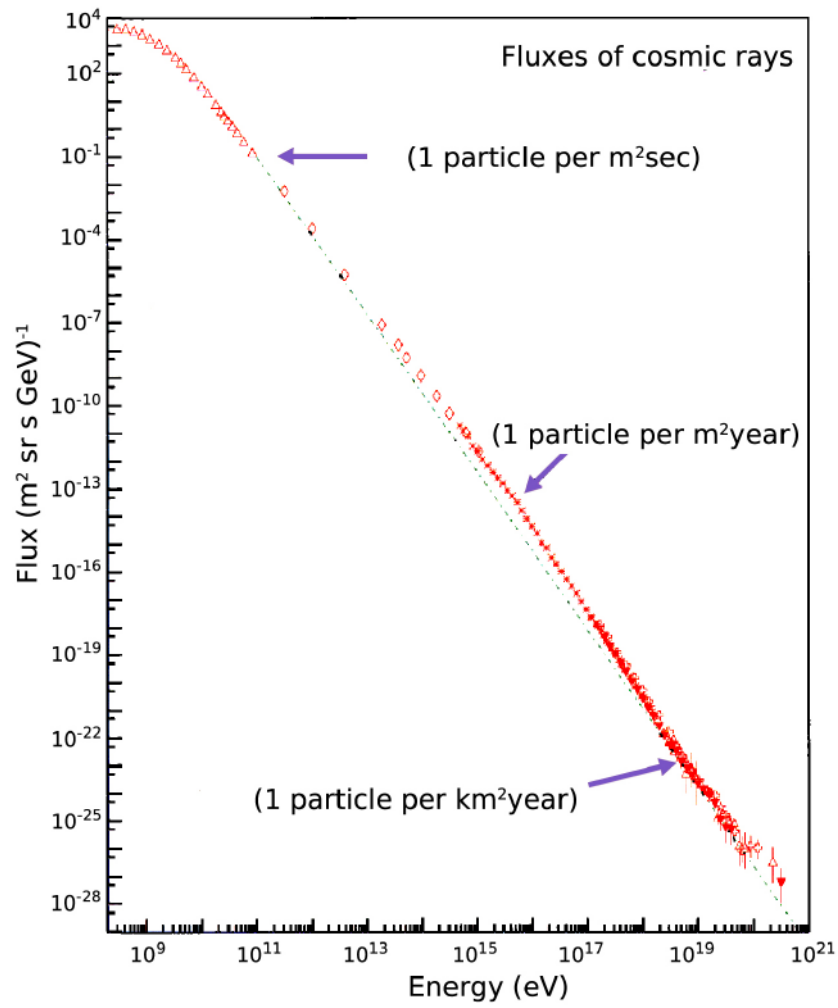


Figure 3.1: The flux of cosmic rays as a function of the energy

$$\begin{aligned}\pi^+ &\rightarrow \nu_\mu + \mu^+ \\ \mu^+ &\rightarrow \bar{\nu}_\mu + \nu_e + e^+ \\ \pi^- &\rightarrow \bar{\nu}_\mu + \mu^- \\ \mu^- &\rightarrow \nu_\mu + \bar{\nu}_e + e^-\end{aligned}\tag{3.4}$$

$$\tag{3.5}$$

Because the mechanisms that produce CRs can produce also neutrinos and high-energy photons through π_0 decay, gamma-ray sources are in general also good candidates for neutrino sources. Nevertheless alternative mechanisms that produce high energy photons like synchrotron radiation can be present (see section 4.1.1).

In order to prove that a source is a CR accelerator one can therefore detect high energy gamma-rays coming from that source but with a clear evidence of hadronic origin ([2], [3]), or detect high energy neutrinos. The latter would give a uncontroversial proof of CR production in an astrophysical source.

Various candidates of CR sources have been proposed both from galactic or extragalactic origin.

Supernova remnants (SNRs) are considered to be the most likely sites of galactic CR production. After a supernova explosion the outer part of the former star expands into space and interact with the surrounding material to form a shock front. The presence of strong variable magnetic field produced by the remnant neutron star can accelerate charged particles though Fermi mechanism. Recently the Fermi-LAT satellite has observed a signature of neutral pion decay in supernova remnants [2]. This has been the first direct observation of cosmic-ray production in the SNRs environment. Nevertheless the region around the knee (\sim PeV) in the CR spectrum can not be explained by the lower energy CR production detected by Fermi-LAT. In order to firmly establish the SNR paradigm for the origin of cosmic rays, it should be confirmed that protons are indeed accelerated in, and released from, SNRs with the appropriate flux and spectrum. More details about the search of galactic PeV CR sources (PeVatrons) are given in section 4.6.

Other galactic promising CR sources are binary systems formed by a compact object like a neutron star or a black hole accompanied by a large star. The compact object accretes material from its companion which is accelerated in an accretion disk and partly ejected in jets along its rotational axis. Inside those jets shock fronts can occur and particles can be accelerated. A popular sub-class of binary systems are microquasars.

Finally our Galactic Center (GC) is one of the most interesting region of our Galaxy. Here an intense diffuse emission of gamma-ray with energies greater

than 100 GeV has been observed which likely implies the presence of a source of CR protons and thus of neutrinos. A recent paper by HESS shows the signature of the presence of PeV protons within the central 10 parsecs of the Galaxy. The supermassive black hole Sagittarius A* is proposed to be linked to this PeVatron [3].

Outside our own galaxy up to cosmological distances, sources are typically much larger and they are capable to accelerate particles up to 10^{20} eV but the particle acceleration mechanism and consequently neutrino and gamma production remains the same.

Among the different extragalactic sources, potential particle accelerators are Active Galactic Nuclei (AGN) which are galaxies with supermassive black holes in their center accreting material in a very similar way of galactic binary systems but on a much larger scale (central black holes have typical masses of 10^6 solar masses). Other potential sources are Gamma Ray Bursts (GRB) that are observed as bright transient gamma-ray signals. They are considered as mergers of massive objects (black holes or neutron stars).

3.2 Neutrino detection

The advantage of using neutrinos as astrophysical probes is that, on one side, neutrinos are neutral and thus are not deviated by galactic and intergalactic magnetic fields and, on the other side, they interact weakly with matter and therefore are almost not absorbed during their trip from the source to the Earth. On the other hand their detection is very challenging and requires a large target mass.

The basic principle to build a large volume ($\sim \text{km}^3$) neutrino telescope is a matrix of light detectors (for example PhotoMultipliers, PMTs) inside a transparent medium like water or ice to detect the Cherenkov photons emitted by relativistic charged particles produced by the neutrino interaction.

The high-energy neutrino may interact, in fact, with a single nucleon in the medium surrounding the detector and, in case of a charged current (CC) weak ν_μ interaction, the path length of the final muon may result of the same order or exceeds the dimensions of the detector itself. The measurement of the number and arrival time of the Cherenkov photons produced by this muon in the 3D PMTs array of the detector allows the reconstruction of the track direction. Of course the initial ν_μ and the final μ directions do not overlap but at energies higher than few TeV the difference between the two is below 0.5° , the typical intrinsic angular resolution of a neutrino telescope. All neutrino flavors (ν_e, ν_μ, ν_τ) can be detected by neutrino telescopes but thanks to the larger muon range in respect to the other leptons range, the highest

detection efficiency can be reached by exploiting ν_μ interaction. These detectors are not background free. Showers induced by interactions of cosmic rays with the atmosphere produce the so-called atmospheric muons and atmospheric neutrinos. Atmospheric muons can penetrate the atmosphere and up to several kilometers of ice/water. Neutrino detectors are therefore located deeply under a large amount of shielding in order to reduce the background. The flux of down-going atmospheric muons exceeds the flux induced by atmospheric neutrino interactions by many orders of magnitude, decreasing with increasing detector depth. Therefore the up-going muons can only be produced by interactions of up-going neutrinos and from the bottom hemisphere the neutrino signal is almost background free. Figure 3.2 shows the comparison between data and Monte Carlo simulations of the reconstructed events in the ANTARES telescope as a function of the elevation angle θ . For $\theta > 0$ the reconstructed events are largely dominated by atmospheric muons while for $\theta < 0$ the events are mainly coming from atmospheric neutrinos with a small contamination of misreconstructed atmospheric muons. Only atmospheric neutrinos that have traversed the Earth represent therefore the irreducible background for the search of cosmic neutrinos. Cosmic neutrinos are expected to cluster in the direction of their production source and have an energy spectrum that extends to PeV energies. Atmospheric neutrinos, instead, are isotropic and their energy spectrum stops well below the cosmic neutrino one. Those differences are generally used to distinguish the background from signal neutrinos. The rejection power of atmospheric neutrinos depends therefore both on the pointing capability of the telescope and on the uncertainty in the reconstruction of the parent neutrino energy.

The lower energy threshold for neutrino detection depends on the distance between the photosensors. In the case of ANTARES the low energy threshold is at about $E_\nu = 10$ GeV. At this neutrino energy the produced μ range is around 50 m and the Cherenkov light can be detected by 3 or 4 detection modules (see next section) sufficient for certain track reconstruction algorithms [4].

The upper energy threshold depends on the neutrino absorption inside the earth. Due to the increasing neutrino nucleon cross section, the earth becomes opaque to neutrinos at a certain energy. The mean free path of neutrinos inside the earth becomes equal to the earth diameter at 70 TeV. At 100 TeV vertical neutrinos have transmission probability of 10%. The same probability is obtained for neutrinos of 10 PeV with an inclination corresponding to a zenith angle $\theta = 80^\circ$.

Considering a typical neutrino flux of the form $\sim E^{-2}$, most events would be detected between 10 TeV and 1 PeV.

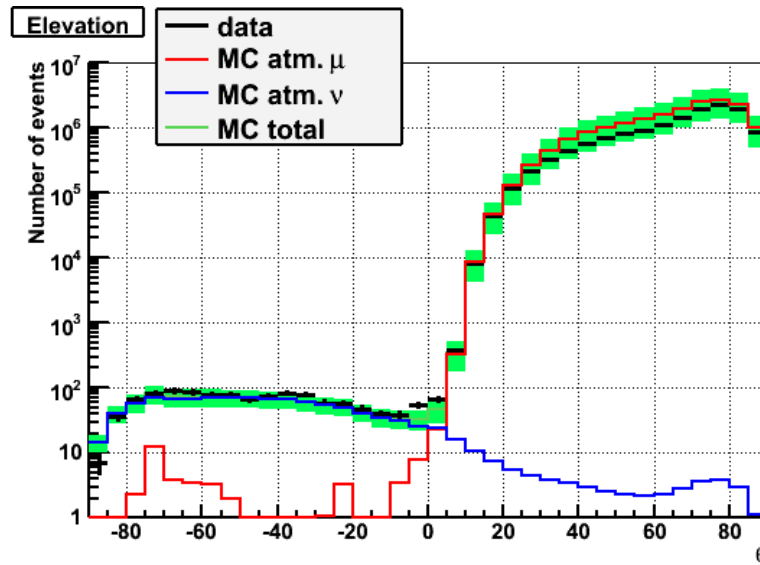


Figure 3.2: Elevation distribution of reconstructed events for the period May 2007-December 2007 and 2008. The Monte Carlo expectations for the atmospheric muon and atmospheric neutrino backgrounds are indicated.

3.3 The ANTARES detector

The ANTARES detector is located at a depth of 2475 m in the Mediterranean Sea, 42 km from La Seyne sur-Mer in the South of France ($42^{\circ}48'N$, $6^{\circ}10'E$). It is equipped with 885 optical sensors arranged on 12 flexible lines. Each line comprises up to 25 detection storeys each equipped with three downward-looking $10''$ PMTs, oriented at 45° from the vertical. Each PMT is installed in a Optical Module (OM) that consists in a $17''$ glass sphere in which the optical connection between the PMT and the glass is assured by an optical gel. The lines are maintained straight by a buoy at the top of the 450 m long line. The spacing between storeys is 14.5 m. The distance between adjacent lines is of the order of 60 m (Fig. 3.3). The three-dimensional grid of photomultiplier tubes is used to measure the arrival time and position of Cherenkov photons induced by the passage of relativistic charged particles through the sea water. The reconstruction algorithm relies on the characteristic emission angle of the Cherenkov light in water (about 43°) to determine the direction of the muon and hence infer that of the incident neutrino.

The first detection line was installed in 2006. Five lines have been operating since March 2007 and 5 more lines were put into operation in December 2007. With the installation of the last two lines in May 2008, the detector construc-

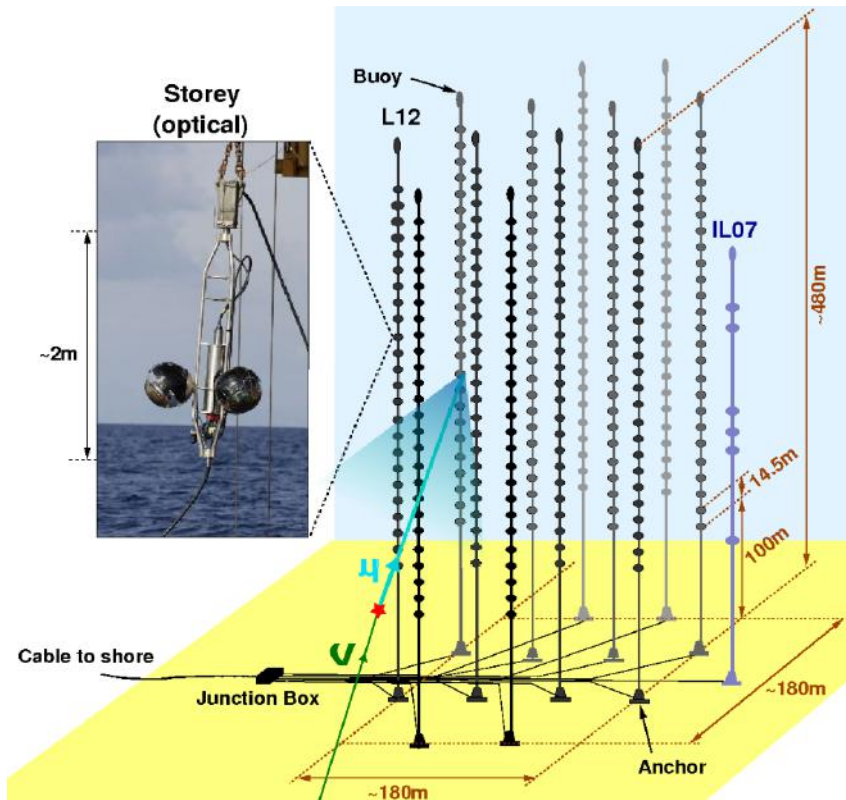


Figure 3.3: Schematic view of the ANTARES detector. The inset shows a picture of the optical storey.

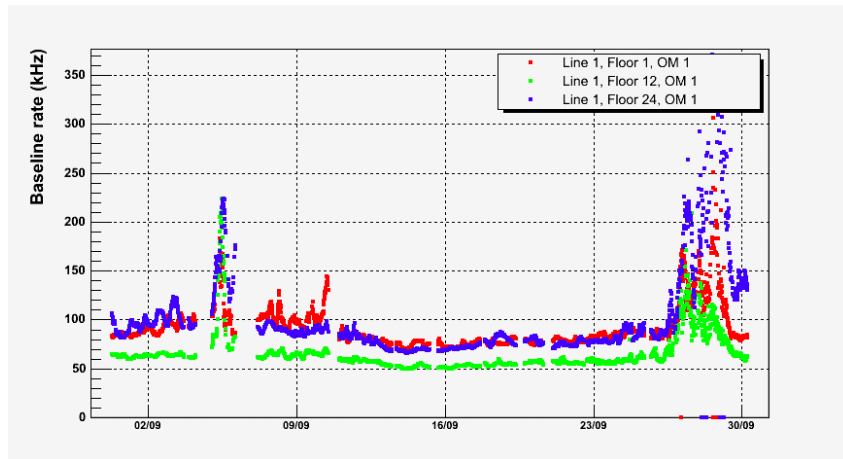


Figure 3.4: Measured background rate for three OM1s of Line 1 at the ANTARES site.

tion was completed. An additional line (IL07) contained a set of oceanographic sensors dedicated to the measurement of environmental parameters.

An average background pulse rate of 70 kHz is measured on each PMT. Figure 3.4 shows the rate measured at the ANTARES site for three OM1s on Line 1. This high background comes mainly from the bioluminescent microorganisms present at the ANTARES site and from the Cherenkov light produced by the electron coming from the decay of ^{40}K present in the salty sea water. On top of this constant rate, one can observe some bursts that increase the rate up to several hundreds of kHz. Those bursts are produced by macro bioluminescent organisms passing close to the PMTs. The rate of these bursts is directly correlated with the sea current velocity that is constantly measured with the instrumentation line.

The ANTARES data acquisition is based on the all-data-to-shore concept [5], in which all hits above a certain threshold (typically set at a level corresponding to 0.3 of the signal expected from a single photo-electron) are digitised and transmitted to shore. Due to the high background rate it is not possible to write all the data flow, which can easily exceed the rate of 1 GB/s, to disk and therefore the data are filtered onshore by a computer farm that applies different trigger algorithms. The typical trigger rate is 5-10 Hz, dominated by downgoing muons. In addition several multi-messenger triggers are implemented in the ANTARES data acquisition. The first is an external trigger generated by the gamma-ray bursts coordinates network (GCN) that causes all the buffered raw data contained in a two-minutes buffer memory to be stored on disk. This offers the potential to apply looser triggers offline

on this subset of the data [6]. An other trigger is an alert which, in case two neutrino-induced events coming from the same region of the sky in a short time window or a very high energy event are detected, is sent from ANTARES to a network of optical telescopes, for an optical follow-up of the potential neutrino source [7]. Moreover ANTARES receives alerts from the SNEWS (SuperNOva Early Warning System) network.

3.4 Calibration of the detector

Between 2008 and 2014 I have been the coordinator of calibrations for the ANTARES experiment. Calibrations are extremely important to ensure the optimal performance of the detector and the quality of the data. One of the main features of the ANTARES detector is the extremely good angular resolution of 0.3° expected at neutrino energies greater than 10 TeV. This relies on good timing resolution and accuracy of the location of the PMTs. The positions of the PMTs are measured every two minutes with a high-frequency long-baseline acoustic positioning system comprising fixed acoustic emitters-receivers at the bottom of each line and acoustic receivers distributed along a line. After triangulation of the positions of the moving hydrophones, the shape of each line is reconstructed by a global fit based on a model of the physical properties of the line and taking into account the information provided by the tiltmeters and compass sensors located on each storey. The displacement of the PMTs depends on the intensity of the sea current. For typical currents of few cm/s the displacement of the top storeys is of the order of few meters. The uncertainty on the positions of the PMTs is of the order of 10 cm [11].

The time calibration of the single PMTs is performed with different systems. A common clock signal is delivered from shore to the whole apparatus. The clock system is also capable of determining the time differences between the different storeys of the detector. The determination of the remaining residual time offsets within a storey, due to the transit time of the PMT and to the front-end electronics, is obtained before the deployment of the line, in a dark room where groups of OMs are illuminated by a common laser source. The time calibration is also performed in the sea by means of a system of optical beacons distributed throughout the detector. During special calibration runs, a LED beacon illuminates the neighbouring storeys on its line. The time correction in respect to the on-shore calibration is obtained by measuring the time difference (time offset T_0) defined as:

$$T_0 = T_{beacon} - T_{PMT} - Delay \quad (3.6)$$

where T_{beacon} is the optical beacon firing time, T_{PMT} is the time at which the

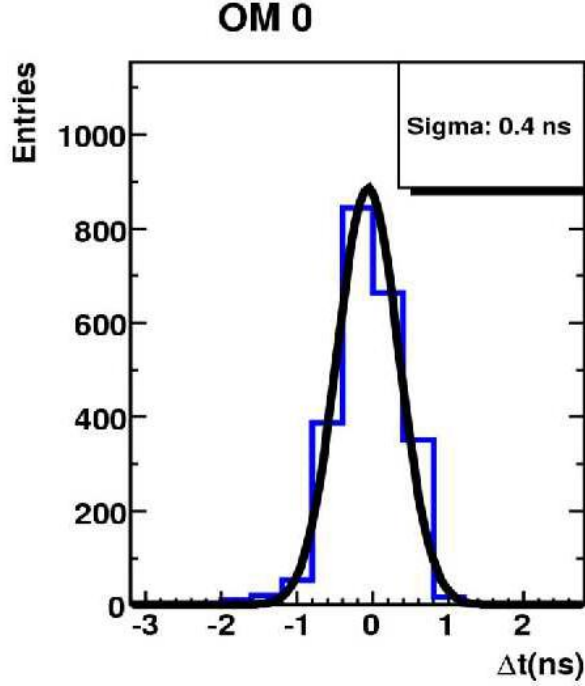


Figure 3.5: Example of T_0 distribution between a PMT and a LED OB. The standard deviation of 0.4 ns can be understood as an estimation of the ANTARES time resolution of the electronics.

light is detected by the PMT and *Delay* is the time needed by the beacon light to reach the PMT. An example of typical T_0 distribution in situ is shown in Figure 3.5. The T_0 peak position can be used to correct the relative timing of each single PMT in respect to the on-shore calibration. The timing calibration between on-shore and in-situ can change for example in the case of changes of PMT high-voltage and threshold settings.

Since the contribution of the transit time spread of the PMT is negligible due to the high intensity of the LED beacon, the resolution of the T_0 distribution in Fig. 3.5 gives directly the time resolution due to the electronics. The latter is of the order of 0.5 ns for all PMTs well within the specification to ensure the optimal angular resolution of the detector [12]. The relative time offsets among lines can be obtained with the laser beacons. Being much more powerful than the LED beacons, the lasers can illuminate all detector lines. The relative time offsets among lines are then computed as the average of the time residual peaks between the laser and the PMT. In addition to the interline calibration, the laser beacon also provides a tool to compute the time offsets

of the OMs in the lowest storeys which are not illuminated by the led beacons in the line.

The ^{40}K present in the sea water is not only background but also an important calibration tool [9]. The decay $^{40}\text{K} \rightarrow e^- \nu_e \text{ } ^{40}\text{Ca}$ yields an electron with an energy up to 1.3 MeV. This energy exceeds the Cherenkov threshold for electrons in water (0.26 MeV), and is sufficient to produce up to 150 Cherenkov photons. If the decay occurs in the vicinity of a detector storey, coincident signals may be recorded by pairs of PMTs on the storey. In Figure 3.6 an example of the distribution of the measured time differences between hits in two OMs of the same storey is shown. A clear peak is found, in good agreement with the expectations from simulations for ^{40}K decay (see section 3.5). The data has been fitted to the sum of a Gaussian distribution and a flat background. The width of these distributions is set by the difference in the distance from the point where the decay occurs to each of the OMs of the pair. The position of the peak can be used to cross-check within each storey the time offsets provided by the onshore dark room and optical beacon calibrations. If the time offset of one of the OMs of the pair were incorrect, we would see that the peak is displaced from zero. The RMS of the mean intra-storey time difference distribution determined by the ^{40}K improves from ~ 0.72 ns to ~ 0.5 ns when using the time offsets calculated in situ rather than those determined from the dark room calibration. It is worth noticing that the ^{40}K intra-storey calibration is independent of the LED OB system and relies on a completely different light source: the ^{40}K is a dim distributed and closeby source, whereas the beacons are powerful, point-like and distant sources.

3.5 The Optical Module acceptance

To determine the sensitivity of the telescope to astrophysical neutrino fluxes, the ANTARES collaboration has developed a simulation code that allows to determine the selection criteria for rejecting atmospheric muon background and identify neutrino events. The simulation code called *km3* [10] is divided into three processes: the physics generation of the events, the Cherenkov light emission and propagation and the detector response. In the last step (detector response) the photon direction and energy is determined and the photon is detected by the OM depending on the OM acceptance. The OM acceptance corresponds to the probability that a Cherenkov photon impinging on the OM with a certain angle with respect to the OM axis and a certain energy is detected. This probability is not calculated directly in the *km3* simulation code but is provided by an external table.

At the beginning of the ANTARES project different measurements were

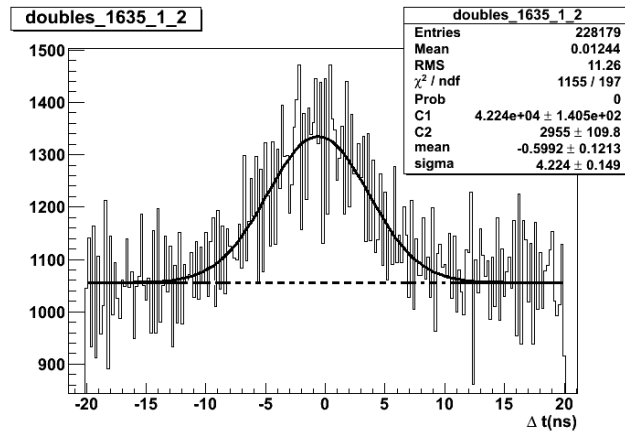
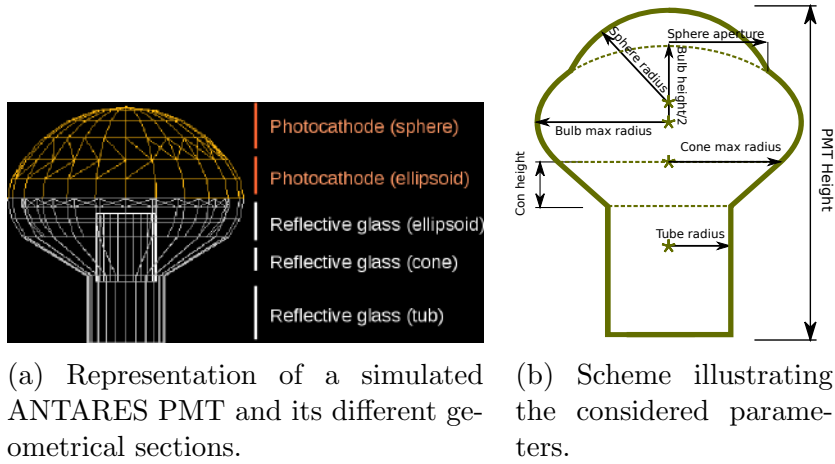


Figure 3.6: Distribution of background hit time differences for one pair of OMs in the same storey. The peak is due to single ^{40}K decays detected in coincidence by two OMs. The data have been fitted to a sum of a Gaussian distribution and a flat background from random coincidences.

performed in a water tank to determine the angular acceptance of the OM. Unfortunately those measurements were affected by large light scattering due to the presence of air bubbles in the water tank. This effect is suppressed in deep sea waters due to the high pressure. The enhanced scattering affects mainly large photon angles mimicking a higher efficiency of the OM at large angles. For this reason a dedicated GEANT4 [13] simulation has been developed to describe the ANTARES OM. This work started in 2008 and has experienced many different phases in both code simulation developments and dedicated lab measurements. In the next section I will give an overview of the work done in the last 5 to 10 years and I will mainly concentrate on the methodology [14]. The reported results are not definitive since the work is, even if very much advanced, still in progress.

3.5.1 Optical Module simulation

The principle of GEANT4 simulation is to use a particle tracking method which takes into account each particle, propagates and interacts it step-by-step in the different media. A detailed description of the OM geometry has been implemented in the GEANT4 simulation. In ANTARES the PMTs are enclosed in 17" pressure-proof glass spheres. The optical contact between the glass sphere and the 10" PMT (Hamamatsu R7081-20) is assured by an optical gel. The refractive index and absorption length of the materials are known [15]



(a) Representation of a simulated ANTARES PMT and its different geometrical sections.

(b) Scheme illustrating the considered parameters.

Figure 3.7: The PMT geometry is constructed by the simulation software using basic geometrical shapes (sphere, cone, ellipsoid, tubes (a)) using the parameters (b).

and implemented in the simulation. Only the OMs of one storey are simulated. They are positioned with the axis of the PMTs pointing outwards and inclined at 45° below the horizontal. The μ -metal grid magnetic protection is not simulated due to its complex structure, hard to implement in GEANT4. Its effect is taken into account in the photocathode efficiency correction described later. The PMT geometry can be reduced to a list of fundamental shapes shown in figure 3.7a, governed by fundamental parameters represented in figure 3.7b. These parameters provided by the constructor are enough to fully constraint the PMT geometry.

To complete the description and reproduce some reflection effects observed in the laboratory [16], the dynode tube has been implemented in the simulation. It is simulated by a cylinder with a rough metallic surface with the dynode's hole, on its top.

One of the crucial points of the simulation is the treatment of the photocathode as a thin metal layer. The ANTARES PMT is coated with a bialkali photocathode [15]. The thickness and refractive index of a typical bialkali PMT have been obtained by a dedicated measurement reported in [17]. The quantum efficiency (QE) depends on the probability for an optical photon to be absorbed by the photocathode and to be converted to a photo-electron. It depends on the photon wavelength (λ) and incident angle (θ), and can be expressed by

$$QE(\lambda, \theta) = P(\lambda) \cdot A(\lambda, \theta) \quad (3.7)$$

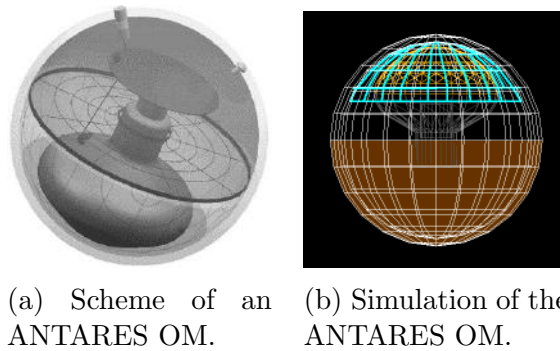


Figure 3.8: Illustration of the OM scheme (left) and simulated geometry (right). The colors correspond to the glass sphere (white), the gel (cyan) and the absorber (brown) and the PMT (gray and yellow).

where $A(\lambda, \theta)$ is the absorption probability and $P(\lambda)$ the conversion probability of an absorbed photon into a photo-electron. This QE has been provided by Hamamatsu for a beam hitting the center of the PMT at an incident angle of $\theta = 0^\circ$ [18]

In the case of a PMT in air, the range of incident angles of the photon on the photocathode is limited due to the high refractive index difference between the glass of the PMT and the air. Therefore, in air the value provided by Hamamatsu ($QE(\lambda, \theta = 0^\circ)$), is enough to define the PMT quantum efficiency for any incident angle. On the other hand, for the studied case of an OM immersed in water, the succession of similar refractive indices interfaces (water, glass of the OM, optical gel, glass of the PMT, photocathode), allows a range of large incident angles on the photocathode. This implies that the angle dependence of the QE can not be neglected.

The QE depends on the photon path length in the metal layer, via:

- the thickness of the photocathode (tens of nm) which produces interferences (construction and destruction of the photon waves), not managed by GEANT4,
- the absorption of the photocathode, based on a non-zero complex value of its refractive index.

GEANT4 is able to simulate a layer with a complex refractive index as a surface. It calculates the reflection and transmission angles, but not the absorption probability. A second simulation solution in GEANT4 is to define the photocathode as a volume with an absorption length, but unfortunately a complex refractive index can not be defined for a GEANT4 volume.

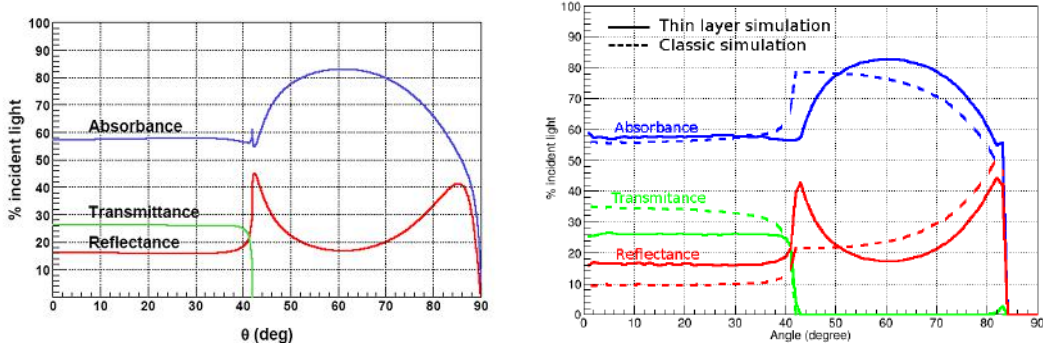


Figure 3.9: Comparison of the absorbance, reflectance and transmittance of the photocathode predicted by the optical model for thin layers presented in [17](left) and the GEANT4 simulations (right) with and without the present optical thin layer extension. The assumed parametrization is $n_1=1.5$ (external medium), $n_2=1.51$ (glass), $n_3=2.7+1.5i$ (photocathode), $n_4=1$ (vacuum); photocathode thickness=20 nm; $\lambda = 442nm$.

The present approach calculates the transmittance, reflections and absorption in the photocathode from the complex refractive index in the case of thin layers. It has been integrated as an extension of the GEANT4 optical boundary and is activated on interfaces where a thin layer with a complex refractive index is present.

This implementation is based on precedent works. In a first study [17] the optical model that combines complex refractive index and thin layer optics has been developed. It has been applied to a bialkali photocathode obtaining its refractive index (real and complex components) and its thickness. Subsequently this model has been adapted to the Auger PMTs [19].

Figure 3.9 shows the results of the GEANT4 simulation, with and without the present extension, for the absorbance, reflectance and transmittance in comparison with the theoretical predictions in [17] for a specific layer.

This extension calculates the probability that a photo-electron is produced. To get a measurable signal, this electron should escape from the photocathode to the internal part of the PMT. The electron is generated at a very low energy (2-3 eV), therefore a quasi-random movement in the photocathode can be assumed. Consequently the probability that the photo-electron escapes the photocathode to the inner phototube is dependent on where the photo-electron is produced in the photocathode. Detailed calculation of the escape probability of the photo-electron is in progress [20].

3.5.2 The OM detection efficiency calibration measurements

The total detection efficiency is affected by additional systematic uncertainties, that are hardly simulated with GEANT4:

- non fully simulated passive components (e.g. the μ -metal grid of ANTARES and NEMO);
- the chance to produce a photo-electron depends on the impact point of the photon on the PMT due to the glass/photocathode irregularities (e.g. the photocathode thickness varies from the center to the borders)
- the chance of photo-electron making it to the first dynode stage (“collection efficiency”), which depends on the position of the emitted electron (the collection is more efficient at the center than at the border of the photocathode);
- the amplification and trigger systems: not all photo-electrons reaching the first dynode give a detectable signal.

These uncertainties can be considered effectively using parametrisation obtained by experimental calibration measurements. In order to calibrate the OM efficiency, two important physical inputs are used:

- the relative detection efficiency of a photon arriving at a certain position on the OM in respect with the detection efficiency of a photon arriving at the top of the OM (relative angular efficiency);
- the absolute detection efficiency of the OM.

Both relative and absolute detection efficiency have been measured in air and in the laboratory. The simulation is therefore first calibrated using air as an external medium, and then applied to seawater. The simulation is finally cross-checked by on-site ^{40}K natural decay measurements.

In laboratory, both measurements (angular and absolute efficiency) have been performed with the same setup at ECAP (Erlangen) and at APC (Paris) [16]. Black boxes were designed to contain an OM, a light source and motorised arms. These arms allow the movement of the light source around the OM, which is fixed on an optical table, at the bottom of the box.

The light source consists of a sphere equipped with a matrix of Light Emitting Diodes (LEDs) with a mean wavelength of $\lambda=378$ nm. A small fraction of the light of the diodes can escape from the sphere through a small hole, providing weak and well-calibrated light emission, dominated by single photons (close to the sea experimental conditions).

The relative angular efficiency measurement

For the relative angular measurement, the arm travels around the OM and allows an orthogonal efficiency scan of the OM (figure 3.11a and 3.11b). The measurement was performed on 4 OMs, for a total number of 18 efficiency scans, represented on figure 3.11a. Each dotted line represents an efficiency scan. The statistical error of each scan is included in the thickness of the line. The large peak observed at about 55° is due to reflection on the interface between the gel and the air inside the OM. The blue points represent the mean values and the standard deviations of the scans.

To determine the PMT relative angular efficiency, the simulation is set to the same conditions (wavelength, angles, testing medium, choice of OM...) as the experimental setup. As a starting point, the photocathode thickness estimates from [17] is used. Then the simulation is iterated until being able to reproduce the measured results. At each step the difference between experiment and simulation is used to evaluate the correction of the photocathode thickness at each point of the PMT. The results of this procedure are compared to measurements in figure 3.11b. This procedure has been done to reproduce the mean of the efficiency scans, and the standard deviation effect. The black line indicates the simulation reproducing the mean of the efficiency scans. The green and the red lines represent the simulation reproducing the mean of the efficiency scans plus and minus the standard deviation.

The absolute efficiency measurement

For the absolute efficiency measurements, a parallel photon beam is placed in front of the OM covering its full apparent surface, as shown in figure 3.10. The absolute efficiency is obtained by simply counting the number of detected photons with respect to the number of photons emitted by the calibrated light source. These measurements have been performed on two ANTARES OMs. The results from the two OM measurements are consistent with the statistical errors. The absolute efficiency calibration provides a scale factor to the total efficiency of the simulated OM.

The simulation was performed reproducing the experimental conditions. By comparing the simulation results with the calibration measurement results, the absolute OM efficiency from simulation had to be scaled down by 20% to be able to reproduce the calibration measurement.

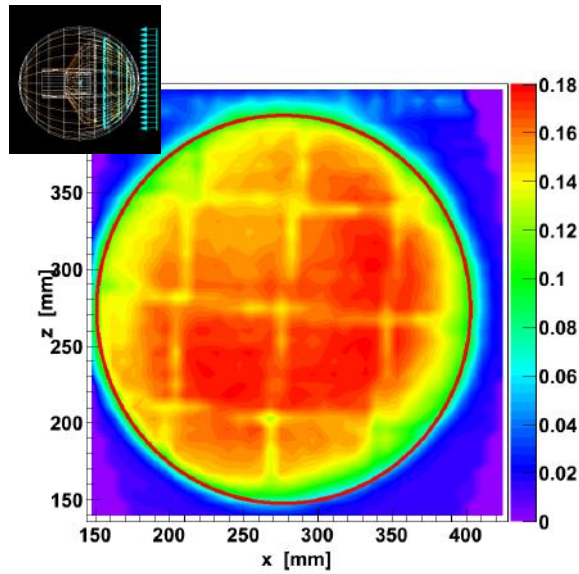


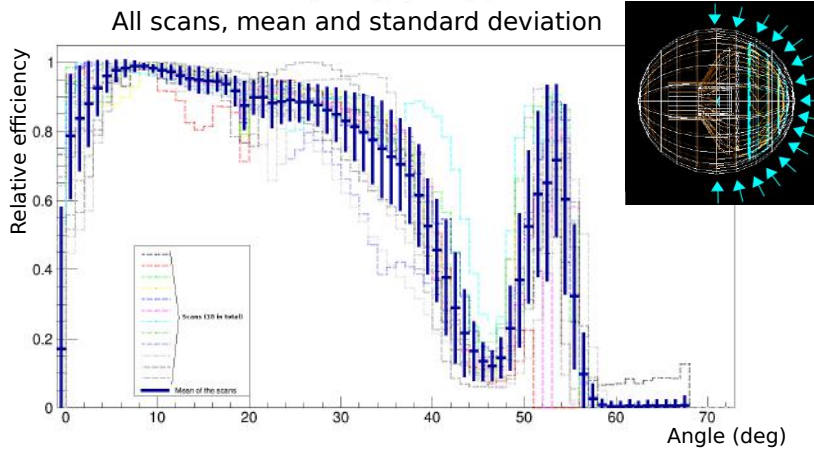
Figure 3.10: Results of the parallel beam scan on an ANTARES OM. The presence of metallic grid can be noticed. A reduction of the efficiency at the center and at the borders of the photocathode is visible.

3.5.3 Potassium 40 decay rate in the sea

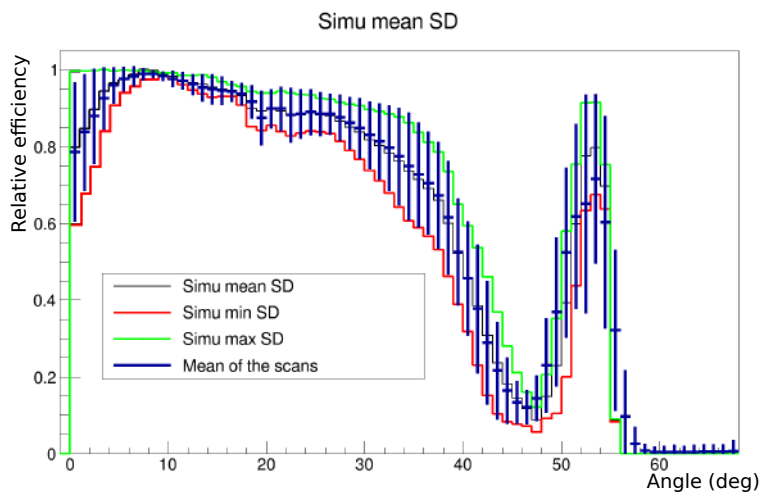
The radioactive isotope ^{40}K , which has a lifetime of 10^9 years, is naturally present in seawater. Thanks to the near-constant salinity in the sea, the exact ^{40}K decay rate can be easily calculated. The salinity at the ANTARES site is 3.845 % with a proportion of 0.013 % of natural ^{40}K . It represents an activity of $13,750 \text{ Bq/m}^3$ representing 11.2 % of 1.5 MeV gamma-ray emission from electron capture, and 88,8 % of 1.3 MeV β^- decay. It has been already shown that the ^{40}K decay is used in ANTARES to cross-check the time calibration. Moreover this decay can be used as a calibration source to cross check the efficiency of the OM (see section 3.4).

The coincidence rate has been continuously measured by ANTARES [9]. Therefore, by performing a simulation using the experimental condition of the ANTARES site, it is possible to directly compare experimental and simulated results and therefore to obtain an absolute calibration of the OM.

The calibration is based on the measurement of the coincidence rate between two close OMs of the same floor. The analysis excludes the bioluminescence background and is almost independent of the water properties (only nearby decays produce coincident events in two PMTs). The experimental value for the ^{40}K coincidence rate is about 16 Hz. Simulated coincidence rate has been obtained and reasonably agrees with the experimental value. How-



(a) Scans of the OMs (dotted colored line, 18 in total) and mean of the scans (dark blue). The error bars correspond to the standard deviation of the scans about the mean for each angle.



(b) Mean of the scans (dark blue) and simulation results (black). The green and red lines represent the simulation reproducing the mean of the efficiency scans plus and minus the standard deviation.

Figure 3.11: Results of the OMs scans (data and simulation).

ever a final value can not be given yet since the work is still in progress. As underlined at the beginning of the section, the OM simulation code has been revisited several times and small modifications and corrections have been done. The ^{40}K rate depends dramatically on even small corrections since the efficiency enters quadratically in the coincidence rate determination.

3.5.4 Conclusion and perspectives

The new determination of the acceptance using the GEANT4 detailed simulation has been recently implemented in the ANTARES Monte Carlo simulation together with other changes that have significantly improved the quality of the simulated data allowing to put some constraints on a critical parameter for the ANTARES detector namely the water absorption length.

The GEANT4 code has been also applied to the KM3NeT Digital Optical Module (DOM). In respect to the ANTARES OM in which a big 10" PMT is contained in a glass sphere and three OMs form a storey, the new DOM is formed by 31 3" PMTs contained in a glass sphere. The DOM has been simulated and data-monte carlo comparison of ^{40}K coincidence rates between 2 and more 3" PMTs in the same DOM has been done obtaining good agreement [14]. As already mentioned the fine-tuning of the simulation in terms of detailed description of the photoelectron behaviour in the photocathode is in progress and new updated results are expected soon [20]

3.6 SN neutrino detection

Using the GEANT4 code described in previous section we have performed a study to determine the ANTARES sensitivity to a low energy neutrino signal coming from a SuperNova (SN) explosion [23].

3.6.1 Introduction

SN explosion is occurring for stars which are heavier than Chandrasekhar's limit (1.38 solar mass). It's a fast conversion to a neutron star when the thermonuclear processes can't withstand to the gravitational force. During the explosion about 99% of the gravitational binding energy radiates in neutrinos. About 1% are electron neutrinos from the initial "neutralization" phase while the residual 99% are produced during the cooling phase through weak interactions in the hot and dense matter. The latters are roughly equally distributed among all flavours in ν - $\bar{\nu}$. The time scale of this process lasts over tens of

seconds and about one half of the neutrinos escapes the star during the first 1-2 s.

The famous supernova explosion in 1987 occurred in the Large Magellanic cloud (SN1987A) and it was seen by the Cherenkov detectors Kamiokande II and IMB and by the scintillation detectors Baksan and LSD. The ANTARES neutrino telescope could provide the opportunity to detect the Cherenkov light produced by positrons from SN antineutrinos via the reaction $\bar{\nu}_e + p \rightarrow n + e^+$. The signature of this event is a simultaneous increase of the counting rate in the detector. The order of magnitude of the SN antineutrino energy is 10 MeV.

3.6.2 Simulations

For the SN study we have simulated the full 3 OMs ANTARES storey configuration and we used the positron energy spectrum and flux obtained averaging in time the distributions from the model 57 of A.Burrows [24] for a SN1987A like event at a 10 kpc distance.

As a result we have obtained an excess of 14 hits in a 105 ms time interval on each OM. The time interval of 105 ms was chosen because it both corresponds to the standard time slice of the data flow in ANTARES detector and to the time interval of the SN explosion where the highest neutrino flux is produced according to [24]. To fully exploit the geometry of the ANTARES detector, we have also obtained the number of coincidences produced by the positrons light between two or three OMs of the same storey in a 25 ns time window. The motivation to use coincidences between OMs is to decrease the effect of bioluminescence background. For double coincidence rate we have obtained an excess of around 10 coincidence hits in all ANTARES detector in a 105 ms time interval. To evaluate the number of hits from an event at a distance R different from the 10 kpc we used a simple proportion, knowing that $\Phi * 4\pi R = const$.

3.6.3 Supernova signal for coincidences between OMs

The ANTARES configuration allows the light from ^{40}K decay to be simultaneously seen by a couple of OMs in a storey (see section 3.4).

Figure 3.12 represents the time difference between two OMs of the same storey. A plateau, due to the random coincidences in the time window τ of 20ns and a Gaussian shaped distribution, due to ^{40}K decays seen by both OMs (later we call them true coincidences to distinguish from the random coincidences) can be noticed. To extract these two components the distribution was fitted with a Gaussian plus a constant. The rate of the true coincidences extracted from the fit is about 16 Hz for a couple of OMs and it is independent from the

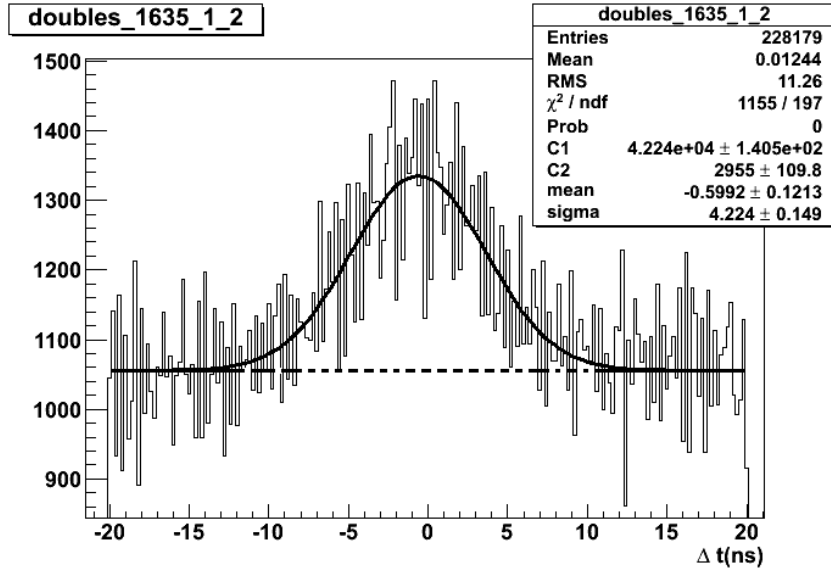


Figure 3.12: Example of the time coincidence distribution for storey 1635, OM 1 and 2. Dashed line represents random coincidence level. The area of the Gaussian accounts for the number of hits from ^{40}K coincidences.

bioluminescence activity. The rate is thus stable in time, but it depends from the couple of OMs since efficiency of the OMs is different.

To understand how the uncertainty on the true coincidence rate from the fit depends on the statistics i.e. on the number of the summed time slices, we performed a simple simulation of the time difference distribution for one couple of OMs assuming an 80 kHz random background on each OM and a Gaussian distribution with 16 Hz for the coincidences. These simulations gave the uncertainty on the extracted true coincidence rate as reported in fig.3.13 for various number of time slices N_{TS} .

To determine the significance of SN neutrino detection we compared the global rate of the coincidences in the detector at any time slice with the sum of the rates of each couple obtained with large number of precedent timeslices to have a good precision as shown in Fig. 3.13. The global detector rate was determined from the time differences between all coincidence hits of every OM couple that were collected in a given timeslice. This distribution was then fitted with the same procedure described above and the error evaluated as in fig.3.13 where the number of couples instead of the number of time slices was assumed. The true coincidence detector rate, $f_{time-slice}$ extracted from the fit is stable in time and equal to the sum of the every OM couple rates in case of no SN explosion or higher in case of SN explosion.

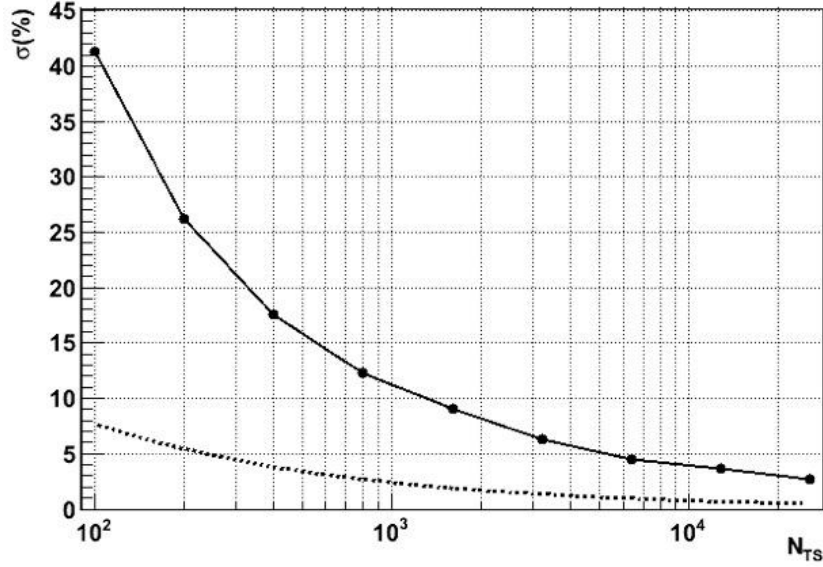


Figure 3.13: Uncertainty on the coincidence rate extracted from the fit of the simulated distribution for different time slice numbers (solid curve). Dotted curve represents error in absence of the random background.

We verified this procedure on real data. To this purpose one period with a 450 OM couples was analysed and the rate for every couple was calculated from 20000 time slices of the data to provide as seen from fig.3.13 an uncertainty less than 5%. The global detector true coincidence rate was then obtained from the fit for every time slice. The difference between this rate $f_{time-slice}$, and the sum of the true coincidence rates of every couple i f_{couple} was evaluated and normalized to the number of couples $N_{couples}$.

$$f_{\Delta-Double} = \frac{f_{time-slice} - \sum_{i=1}^{N_{couples}} f_{couples}^i}{N_{couples}} \quad (3.8)$$

The distribution of this difference for 450 time slices is shown in Figure 3.14. As expected, the distribution of this normalized difference has a mean 0 and sigma 17%, in good correspondence with the expected error from fig.3.13 for 450 N_{TS} .

At the time when this analysis was performed [23] the GEANT4 simulation code was still not optimized and an estimation of a value of 22 Hz for the true coincidence rate was found. The experimental value for the coincidence rate is around 16 Hz. The discrepancy found at that time between Simulation and data was mainly due to the uncertainty in the knowledge of the collection efficiency of the PMT (see section 3.5).

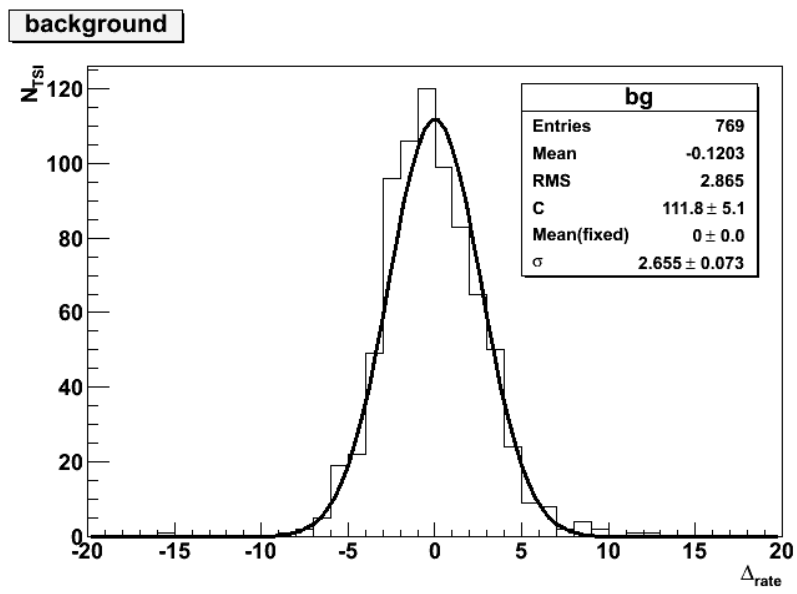


Figure 3.14: Distribution of the $f_{\Delta-Double}$ (see equation 3.8).

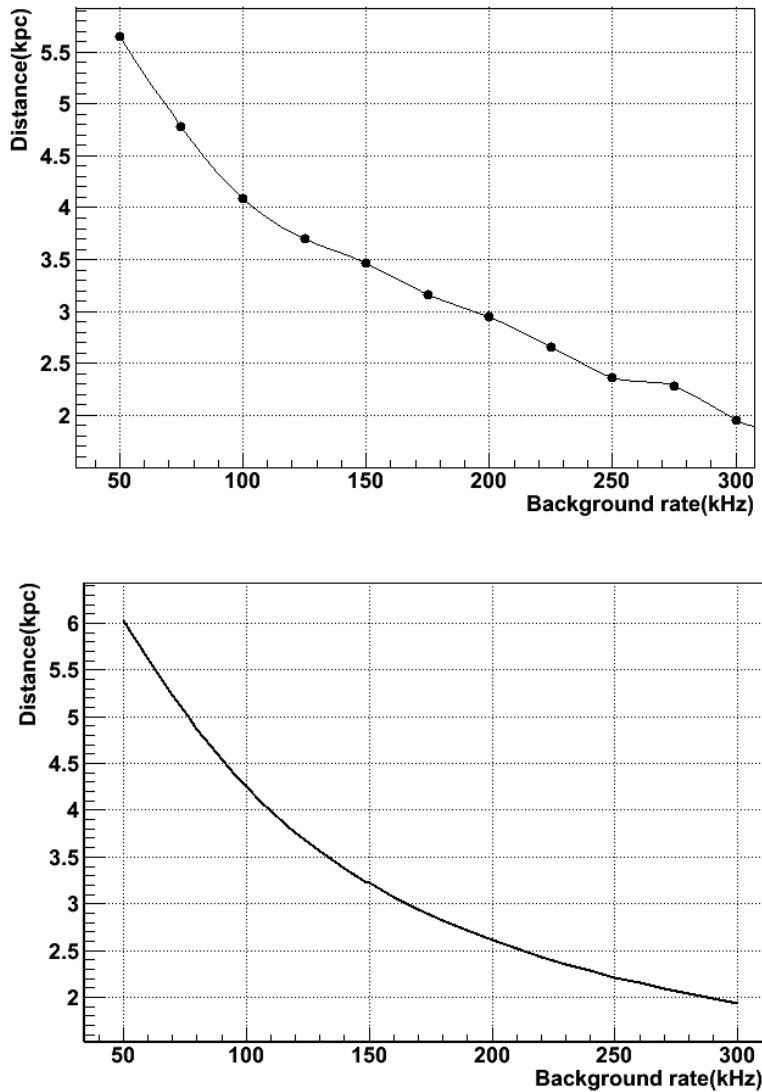


Figure 3.15: Simulated 5σ significance as a function of SN distance and background rate for the double (top) and a triple coincidence (bottom) methods.

The 5σ significance obtained from the simulations of 900 OMs detector is reported in fig.3.15 (top) as a function of the SN distance for various bioluminescence rates.

Given the ANTARES geometry, a triple coincidence in each storey can occur whenever a single event (light from a track, a ^{40}K decay) is simultaneously seen by the 3 OMs. In our approach we require that at least one hit for each OM is detected during a 20ns time window. This means also that in every pair

of the hits in the triple coincidence, the time difference is less than 20 ns. In order to obtain the time difference distribution like for doubles it was decided to use three dependent distributions: $t_1 - t_2$, $t_2 - t_3$ and $t_3 - t_2$, where t_i is time of hits from OM i . In this case the random coincidences do not form a plateau in the time difference distribution but rather a triangular shape. This is because, for example, the difference $t_1 - t_2$ is constrained by the condition that both t_1 and t_2 must be close to t_3 by less than 20 ns.

The fit is thus done adding the Gaussian of the true coincidences to the random triangular part. True coincidences rate for the storey is calculated as a mean value of the true coincidence rates extracted from the fit of the three distributions $t_1 - t_2$, $t_2 - t_3$ and $t_3 - t_2$.

To find the true triple coincidence rate, one month of data was analysed. It was found that the mean storey rate is about 0.065 Hz and it is stable during 3 months. Simulations with GEANT4 gave a higher value: 0.2 Hz. This large discrepancy could be explained considering the already observed behaviour in the double coincidence case where the simulations gave a value around 22 Hz against the observed 16 Hz. In case of a triple coincidence this inefficiency was additionally amplified. The GEANT4 simulation also estimated the total number of triple coincidences from SN to about 0.035 per storey in a time slice. Assuming the same damping in the detection efficiency as for ^{40}K rates (0.2Hz MC against 0.065 Hz experimental), the SN triple coincidence rate was expected to be about 0.11Hz.

Similarly to the double, the coincidence rate of the triple coincidences in the detector during one time slice was calculated. Since the number of triples is much less than the doubles, the fitting procedure was not applicable to the time difference distribution for one time slice. To obtain the significance both true (^{40}K) coincidence rate and random coincidence rate have to be taken into account. Similarly to the double coincidence $f_{\Delta-Double}$ quantity, $f_{\Delta-Triple}$ is defined as:

$$f_{\Delta-Triple} = \frac{f_{exp} - \sum_{i=1}^{N_{storeys}} (f_{^{40}\text{K}}^i + 3\tau^2 f_1^i f_2^i f_3^i)}{N_{storeys}} \quad (3.9)$$

where f_{exp} is the total triple coincidence rate (^{40}K + random) of the detector in a time slice, $f_{^{40}\text{K}}^i$ is the ^{40}K triple coincidence rate for the storey i obtained from a month long period and f_1^i , f_2^i and f_3^i are the single rate in a storey i of OM1,2 and 3 respectively obtained in a time slice.

The simulated 5σ significance as a function of the SN distance and background is shown in the fig.3.15 (bottom).

In order to enhance the probability to detect low energy neutrinos from a Supernova explosion, ANTARES receives alerts from the SNEWS network.

The SNEWS (SuperNova Early Warning System) project involves an international collaboration of experimenters representing current supernova-neutrino-sensitive detectors. In the case of a coincidence detection of neutrinos coming from a core-collapse Supernova by different detectors, the SNEWS network sends an alert. The latency time between the SN event and the generated SNEWS alert could range up to 10 minutes. Therefore in the case of a SNEWS alert, ANTARES will store on disk 30 minutes of coincidence data between the OMs.

3.6.4 Perspectives

In the next years a new larger detector will be built in the Mediterranean Sea namely the KM3NeT detector. It will consist of two blocks. One block (ORCA) will be located close to the actual ANTARES site in the South of France and will be dedicated mainly to fundamental physics, namely neutrino properties determination using the atmospheric neutrino flux. It will have a compact layout and an instrumented volume similar to the ANTARES detector. The second block (ARCA) will be located south of Sicily and will be dedicated to astrophysical neutrino detection. The layout will consist of several lines forming an instrumented volume of 1 km^3 in the first phase and several km^3 in later phases [25]. Both blocks will have the same optical units: the DOM [21] (see section 3.5.4).

Sensitivity studies of SN detection using both ORCA and ARCA have been performed [26, 27]. The same coincidence technique described previously has been adopted but considering multiple coincidences (≥ 3) between several 3" PMTs in the same DOM. Thanks to the larger multiplicity it seems possible to decrease the effect of background coming from ^{40}K but contribution from down-going μ s has to be taken into account. ^{40}K decays produce in general events with fewer coincident hits in a DOM comparing to SN events. Muons produce even harder coincidence spectrum. This correlates with the lepton energies ($1.3\text{MeV } e^-$ for ^{40}K , $10 \text{ MeV } e^+$ for SN and MeV-GeV energies for μ). Very recently a μ -rejector has been developed in the KM3NeT collaboration [27] that exploits the fast μ s time correlation of μ s. A first estimate shows the possibility to detect a SN explosion with 5σ significance until a distance of 36 kpc for ARCA (all Milky Way) and 24 kpc for ORCA.

Bibliography

- [1] M. Spurio. *Particles and Astrophysics-A Multi-Messenger Approach*. In: Springer International Publishing Switzerland (2015).

- [2] M. Ackermann et al., *Science* 339, 807 (2013).
- [3] A. Abramowski et al., *Nature* 531, 476 (2016).
- [4] J. Brunner, HDR Thesis Aix-Marseille Universite , (2009).
- [5] M. Bouwhuis et al., Proceedings of ICRC2009, arXiv:0908.0811
- [6] M. Bouwhuis et al. Proceedings of ICRC2009, arXiv:0908.0818
- [7] D. Damien et al. Proceedings of ICRC2009, arXiv:0908.0804
- [8] A. Heijboer et al. Proceedings of ICRC2009, arXiv:0908.0816
- [9] The ANTARES Collaboration, *Astrop. Phys.* 33, 86 (2010).
- [10] The ANTARES Collaboration, *Astrop. Phys.*34, 179 (2010).
- [11] The ANTARES Collaboration, *JINST* 7 T08002 (2012).
- [12] The ANTARES Collaboration, *Astrop. Phys.* 34, 539 (2011).
- [13] J. Allison et al., *Nucl. Instrum. Meth. A* 835,186-225(2016).
- [14] C. Hugon, Proceedings of ICRC2015, PoS ICRC2015, 1106 (2016).
- [15] ANTARES collaboration, *Nucl. Instrum. Meth. A* 484, 369-383 (2002).
- [16] A. Creusot et al., *Nucl. Instrum. Meth. A* 725, 144-147 (2013).
- [17] D. Motta and S. Schönert *Nucl. Instrum. Meth. A* 539, 217 (2005).
- [18] D.Motta private communication
- [19] A. Creusot and D. Veberi; *Nucl. Instrum. Meth. A* 613, 145 (2010).
- [20] V. Kulikovsiy and C. Hugon private communication
- [21] Kavatsyuk et al., *Nucl. Instrum. Meth. A*, 695, 338(2012).
- [22] Conceptual Design report for KM3Net Infrastructure, April (2008).
- [23] V.Kulikovskiy, Proceedings of ICRC2011
- [24] A. Burrows, *Astroph. J.* 334, 891 (1988).
- [25] KM3NeT Collaboration, "Letter of intent for ARCA and ORCA", (arXiv:1601.07459v2) (2016).
- [26] M. Colomer et al., in *Proceedings of ICRC2017* PoS(ICRC2017)983.

- [27] M. Colomer and M. Lincetto, Proceedings RICAP2018 (to be published)
- [28] A. Roberts et al., Rev. Mod. Phys. 64, 259(1992).
- [29] R. Wischnewski et al., Int. J. Mod. Phys. A, 20 6932 (2005).
- [30] B.K. Lubsandorzhev, Nucl. Inst. and Meth. A 610 68 (2010).
- [31] A.Achterberg et al., Phys. Rev. D 76 027101 (2007).

Chapter 4

Astroparticle physics: CTA

When I arrived at CPPM in 2010 I joined the gamma astrophysics group that had just started its activity the same year. The group was mainly formed by former ANTARES collaborators and the aim was to enlarge the astroparticle activity at CPPM related to the research of the origin of high energy cosmic rays beyond the neutrino astrophysics activities with ANTARES and KM3NeT. Gamma-rays and high energy neutrinos are indeed strictly correlated since they can be produced in astrophysical sources through hadronic processes.

4.1 Gamma-Rays

Gamma-rays are the most energetic form of electromagnetic radiation and the gamma-ray waveband includes photons whose energies are above 100 keV. Figure 4.1 illustrates the Fermi Gamma-Ray Space Telescope [1] all-sky survey after five years of operation for gamma-rays at energy above 1 GeV and below 300 GeV.

The colour intensity corresponds to the brightness of the gamma-ray sources. The diffuse glow prevalent along the Milky Way plane is visible together with many discrete gamma-ray sources both close to and away from the Galactic plane. These sources are objects such as supernova remnants, pulsars (fast rotating neutron stars) and AGNs. To explain gamma-ray emission by those objects observed in lower energy bands (radio, infra-red, optical, x-rays etc) strong magnetic fields and/or violent shock waves have to be taken into account. Thus one of the key motivations for pursuing gamma-ray astronomy is that it enables to study these extreme environments and hence to better understand the particle acceleration mechanisms.

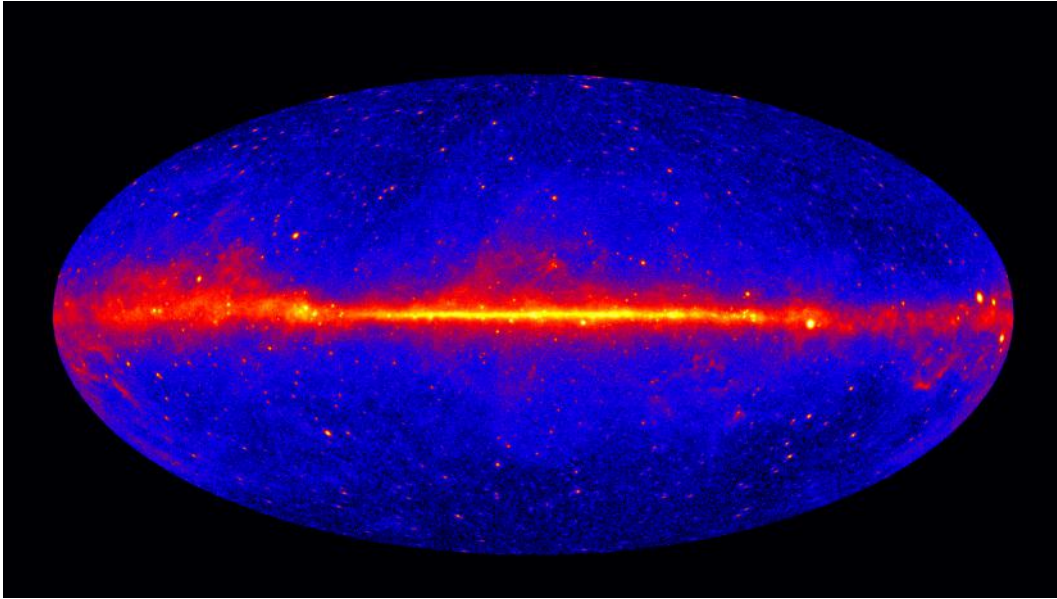


Figure 4.1: The Fermi LAT 5-years sky map with gamma rays with energies greater than 1 GeV. Image credit: NASA/DOE/Fermi LAT Collaboration

4.1.1 Gamma-rays production in astrophysical sources

In section 3.1, a brief description of the Fermi mechanism responsible for the acceleration of charged particles (electrons, protons, heavier nuclei) in astrophysical sources have been given. Particular focus have been put on the acceleration of protons or heavier nuclei since those are the main components of the cosmic ray flux seen on Earth and are responsible for the neutrino production which ANTARES and KM3NeT are aiming to detect. High energy gamma-rays can be produced in both electromagnetic and hadronic interactions. During electromagnetic interactions, gamma-rays can be produced when electrons (and/or positrons) interact with either matter or radiation fields. There are different interaction mechanisms to produce gamma-rays through electromagnetic interaction:

Synchrotron radiation An electron is deviated by magnetic field and produces photon emission. High energy electrons with $E > 10$ TeV produce X-ray radiation in astrophysical sources such as SNRs.

Inverse Compton Scattering (IC) The electron transfers part of its energy to the photon that becomes a gamma ray. Low energy photons present in the process are coming from cosmic microwave background or from environmental star light. It is an important gamma-ray production mechanism and can explain gamma-flux up to tens of TeV. It is

widely believed that this is the primary process giving rise to the high-energy part of the double-bump spectral energy distribution commonly found for AGNs. It is also believed that this is an important gamma-ray production mechanism for pulsars.

Non thermal Bremsstrahlung Electrons can interact with the field of nuclei found in the medium giving rise to GeV to multi-TeV photons. Nevertheless IC scattering is the dominant gamma-ray emission process unless the medium is very dense.

As well as the electromagnetic interactions, gamma-rays can be produced from hadronic interactions as already described in 3.1.

Beam Dump Process When CRs, accelerated to high energies, propagate in the interstellar medium mainly composed by hydrogen, they can interact with matter through inelastic scattering. Charged and neutral pions are produced. The latter decay into gamma-rays.

Photoproduction When CRs, accelerated to high energies, interact with low-energy photons in the surroundings of sources, they produce a Δ^+ resonance which decays into neutral or charged pions 3.1 3.1. The latter decays into gamma-rays.

An important problem in very high energy gamma-ray astronomy is to understand the origin of the gamma-ray emission which can be often explained by both hadronic or leptonic (mainly IC) processes. Figure 4.2 shows the measured high energy gamma-ray flux of one of most brilliant shell-type SNRs: RXJ1713-3946 [2]. As can be seen from the figure both leptonic and hadronic models reproduce the measured flux with the high energy cut-off.

This ambiguity is partly solved at energy above 10 TeV where it becomes easier to distinguish between the hadronic and the leptonic (IC) gamma-ray emission. In fact at these energies the Klein Nishina effect reduces the IC cross-section. Moreover the electron population suffers strong energy losses due to synchrotron radiation. These effects strongly suppress the IC process, unless the gamma-ray emission is associated with strong sources of multi-TeV electrons (i.e. Pulsar Wind Nebulae), observed spectra that extend into tens of TeV without a clear sign of cut-off in their spectrum, strongly favour a hadronic scenario.

In the case of hadronic scenario, with a good approximation, a primary proton accelerated in the source at energy E_p will result in a gamma-ray with energy $E_\gamma = f E_p$, where the conversion factor $f \sim 0.15$ [3]. Therefore, observations of gamma-rays with energies above 100 TeV will probe the spectra of

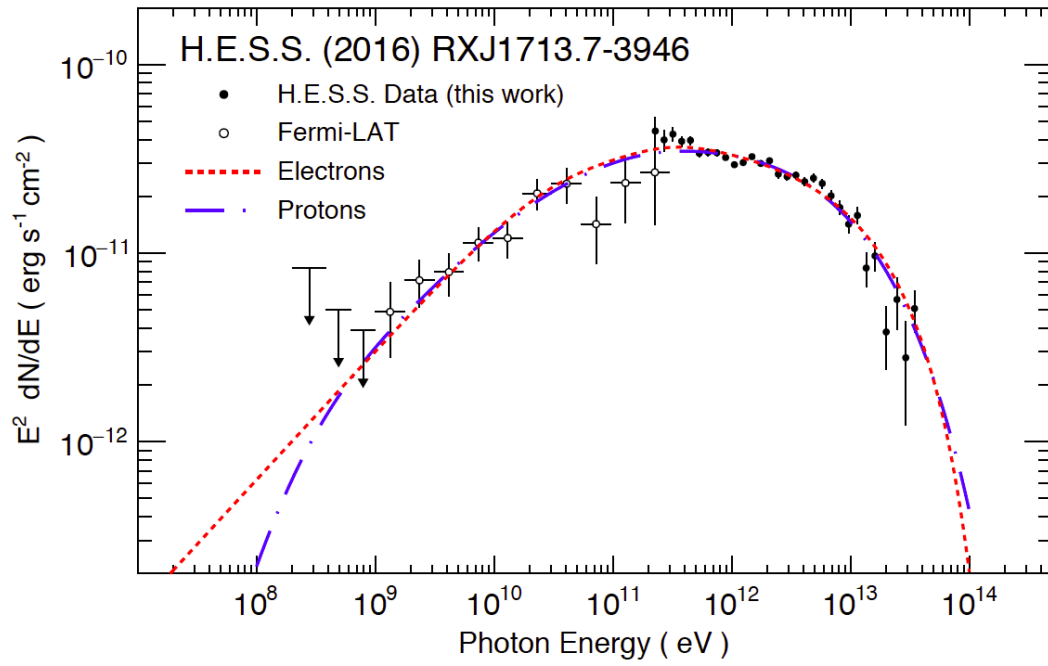


Figure 4.2: Best-fit electron and proton gamma-ray models (broken power laws with exponential cut-offs) are compared to the Fermi-LAT and H.E.S.S. data [2].

protons with energies of the order of PeV, explaining the CR flux in the region of the knee and beyond. More details on the search of PeV cosmic ray sources can be found in section 4.6.

4.2 Attenuation and detection of Cosmic gamma-rays

Gamma-rays produced as secondary particles in astrophysical sources or jets can arrive to the Earth. Gammas are neutral and are therefore not deviated by galactic and extragalactic magnetic fields as it is the case for CRs, but can be attenuated in their trip from the source to the Earth.

One of the largest attenuation processes for VHE gamma-rays is the interaction with low energy photons producing an electron-positron pair. These low energy photons present in the space between galaxies, are known as Extragalactic Background Light of which a component is thought to have been produced by the first stars that have been formed in the early universe. The amount of EBL is indeed connected to fundamental cosmological quantities like the star formation rate density at high redshifts.

VHE gammas can also interact within the Coulomb field of matter to again produce an electron-positron pair. The amount of matter in the path between the source and Earth is small and leads to a minimal attenuation effect of VHE gamma-rays. In comparison, the Earth's atmosphere presents a very dense medium. When the high energy gamma arrives at the Earth atmosphere, it is converted in a electron-positron pair, which in turn produces photons through Bremsstrahlung. These interactions are repeated on and on producing an extensive electromagnetic air shower (EAS) (see Figure 4.3 left).

Cosmic gamma-rays can be detected directly by using gamma-ray detectors mounted on satellites such as the Fermi-LAT satellite [1]. Since high energy gammas are produced by relativistic protons or electrons accelerated through the Fermi mechanism, their energy flux is generally $\propto E_\gamma^{-2}$. Gamma rays at energies until tens to hundreds of GeV can still be effectively detected on satellites. At higher energies the flux is too small and larger detectors should be used which is not feasible for a satellite detector. One can therefore detect cosmic gamma-rays indirectly by measuring the EAS induced by the VHE gamma-ray in the atmosphere by ground based instruments. Two techniques are mainly presently used on the ground: Imaging Air Cherenkov Telescopes (IACT) and Air Shower Arrays (ASA). The latter uses a matrix of particle detectors on the ground to detect directly the particles of the cosmic gamma induced EAS (electrons, positrons and photons). An example of such a cosmic

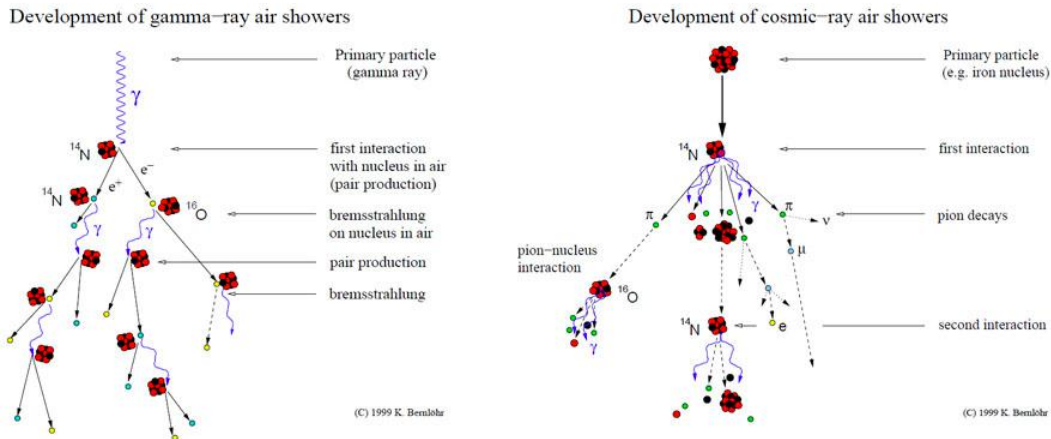


Figure 4.3: Schematic of air shower development. On the left side a gamma-induced shower and on the right side a hadron induced shower are represented. It should be noted the different particle content of the two shower types. In the case of gamma shower only gammas, electrons and positrons are produced along the shower, while for hadron induced showers, other particles like pions and subsequent muons are also produced.

gamma ray detector that has recently started operation is the HAWC (High Altitude Water Cherenkov) gamma-ray observatory [4]. It is composed by an array of 300 large water tanks which detect the Cherenkov light produced by electrons and positrons passing through the water. The advantage of this technique is the large field of view (for example in a 24 hour period HAWC observes two-thirds of the sky) and the permanent observations since the observation doesn't depend on weather conditions. However the angular resolution is not very good as well as the capability to distinguish between electromagnetic showers produced by incoming gammas and hadronic showers produced by CR interacting in the atmosphere which represent the main background source for ground gamma telescopes (see Figure 4.3 right). IACT detectors have, on the other hand, very good angular resolution and gamma-hadron separation power at the cost of a smaller duty cycle and field of view (3° to 5° for present instruments). For IACTS the portion of the visible sky during an observation is indeed quite limited, decreasing the chance of serendipitous discovery of new sources.

The two techniques are therefore complementary and it is generally highly desirable to have both types of instruments for investigating the very high energy gamma-ray sky.

4.3 Imaging Air Cherenkov Telescopes

Electrons and positrons created in EAS induced by high energy gamma-rays are relativistic and are able to produce Cherenkov light which creates a well defined lightpool on the ground (see Figure 4.4). A 1 TeV gamma ray imping on the Earth atmosphere creates a EAS and the Cherenkov light induced by the electrons and positrons arrives in a ring on the ground with a radius of about 120m at an altitude of 2000 m.

The Imaging Air Cherenkov technique is the method used to detect the air showers by observing the produced short-lived Cherenkov pulses of light. The Cherenkov light is collected by the mirror of a ground telescope and focused onto a camera. The Cherenkov light pulses produced in air showers only last for a few nanoseconds meaning the cameras need to perform extremely fast image capture. The camera pixels are sensible to visible light (PMTs for example) optimised for Cherenkov light wavelength (i.e. 300 nm).

Cosmic rays induce extensive hadronic air showers and can be efficiently detected by IACT. Hadronic showers are therefore the principle background source. gamma induced showers are more simmetric than hadronic showers and this feature is used to distinguish between the two types. In Figure 4.5 the image seen on a IACT camera due to a gamma-ray induced shower and a proton induced shower is shown. A gamma-ray induced shower image has generally an elliptical shape while a proton induced shower produces a larger image. Parameterisation of these camera images (for example the width and length of the ellipse which are part of the Hillas parameters [5]) allows for parametric statistical analysis of the images. This provides essential information about the shower enabling for the distinction between gamma-ray and hadronic air showers to reject the cosmic-ray background in the analysis of astrophysical gamma-ray sources.

Current operating IACTs are H.E.S.S., MAGIC and VERITAS [6, 7, 8]. All three telescopes operate more than one instrument (2 for MAGIC, 5 for H.E.S.S. and 4 for VERITAS) that enables the stereoscopic reconstruction of air shower (see Figure 4.4). Looking at the same shower with multiple telescopes improves the determination of the shower-axis orientation in space, the position of the shower core in the observation plane, the angular dimensions of the shower and the depth of the shower maximum. The uncertainty of those reconstructed parameters is therefore significantly reduced in respect to single telescope observations improving the angular resolution. Moreover the use of multiple telescopes allows also for a multiple telescope trigger that improves the background rejection.

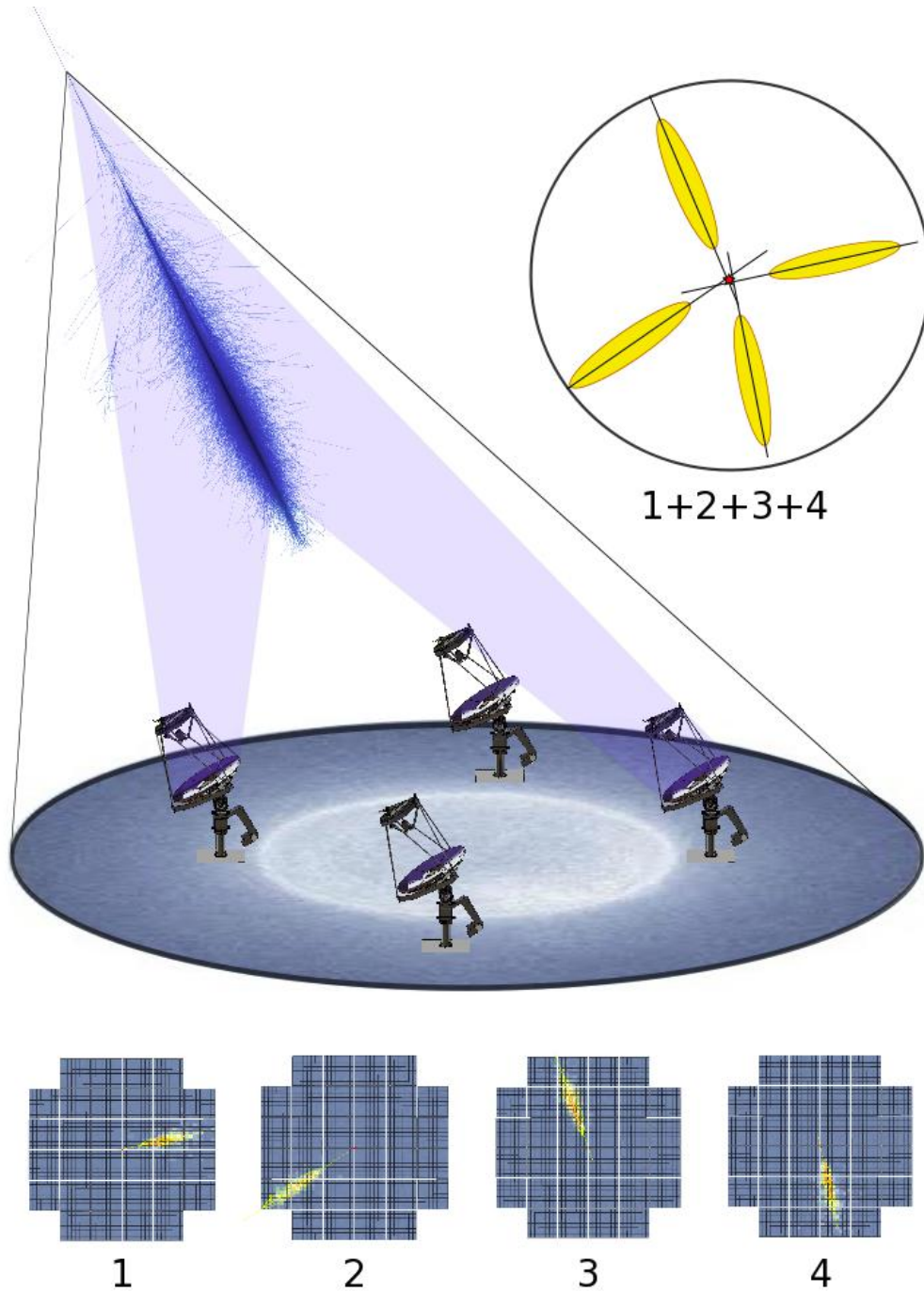


Figure 4.4: Example of detection of a gamma-ray-induced EAS with several IACTs. The pulsed Cherenkov light from the shower propagates towards the ground at an opening angle of $\sim 0.8^\circ$. The EAS is simultaneously seen by 4 telescopes. By using stereoscopy a superposition of four camera images observing the same EAS can be done improving the reconstruction of the shower parameters (Picture credit: T. Armstrong, PhD Thesis)

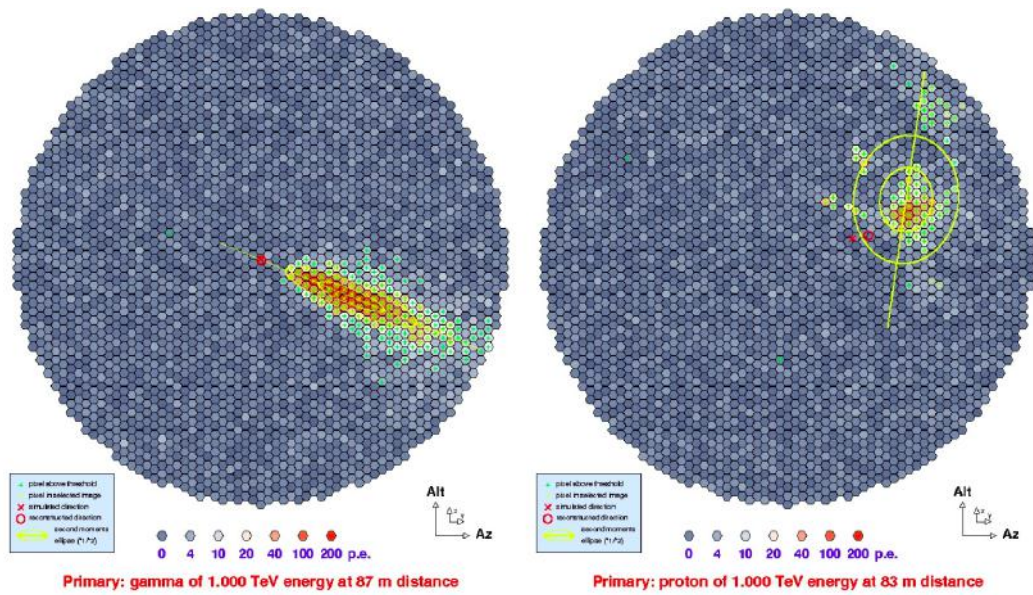


Figure 4.5: A simulated 1 TeV gamma-ray (left) and 1 TeV proton EAS (right) typically captured with the cameras of a ground-based IACT. The gamma-ray (left) has an elliptical shape that points toward the source (red cross) at the centre of the camera, however the proton induced air shower (right) is more dispersed with no certain direction. (Picture credit: C. Rulten, PhD Thesis)

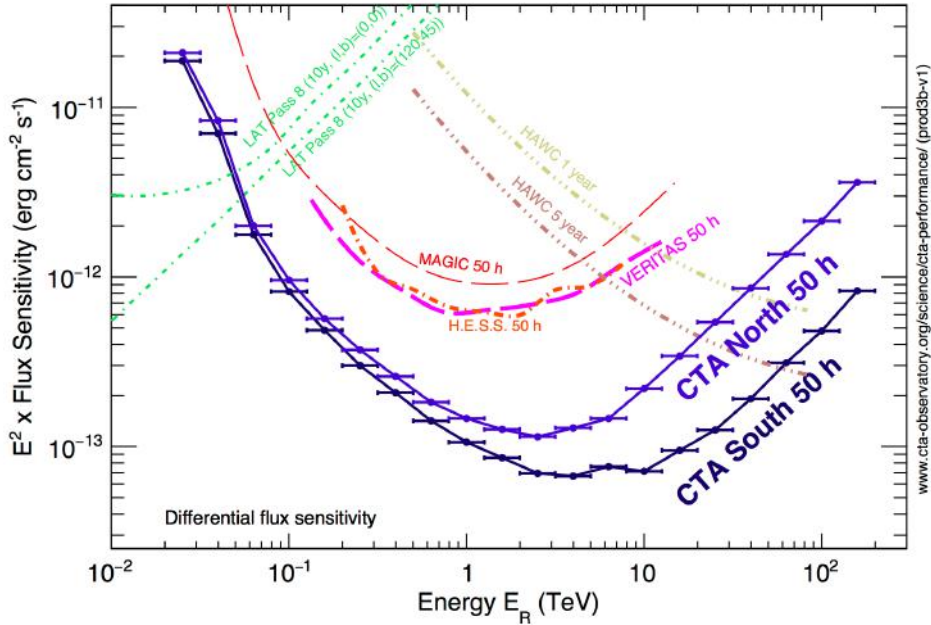


Figure 4.6: Differential sensitivity of CTA (Northern and Southern sites) in comparison with current gamma observatories.

4.4 CTA: Cherenkov Telescope Array

The current generation of IACTs have helped to establish the technique and allowed for the discovery of many astrophysical sources of gamma radiation, both galactic and extra-galactic. By improving the sensitivity and the energy range of the current experiments, it is believed that many more astrophysical sources could be discovered and a better understanding of the already discovered sources could be achieved. The Cherenkov Telescope Array (CTA) is the next generation ground project that will be able to improve current experiment sensitivity by a factor between 5 and 10 depending on the energy region. The expected sensitivity curve is shown in Figure 4.6.

The energy region that will be covered by CTA will go from 20 GeV to 300 TeV allowing in particular to look into the unexplored high energy region above 100 TeV.

CTA will be situated on both the Northern Hemisphere (La Palma on the Canary Islands) and the Southern Hemisphere (Atacama Desert, Chile) in order to cover the entire sky. In order to achieve a broad energy coverage, CTA will use more than hundred IACTs of three different sizes: a Large Sized Telescope (LST), a Medium Sized Telescope (MST) and a Small Sized Telescope

(SST) with a mirror diameter of 23 m, 12 m and 4 m respectively. The need to have three different telescope sizes is driven by the intrinsic nature of the gamma ray energy spectrum of a source which presents a powerlaw spectrum $E^{-\alpha}$ with $\alpha \sim 2$. At low energies ($E < 100$ GeV) the Cherenkov light needs to be sampled efficiently due to the small amount of light coming from low energy showers and therefore large light collectors covering an area of the order of 10% of the light pool are needed. On the other hand at low energies the event rate is quite high therefore the area of this part of the array can be relatively small. CTA foresees 4 LSTs both in the Northern and in the Southern site. The core energy range from 100 GeV to 10 TeV will be covered by the MSTs telescopes. Shower detection and reconstruction in this energy range are well understood from current instruments such as HESS and VERITAS and MSTs will be very similar to such instruments. Improved sensitivity compared to existing instruments will be obtained both by the increased area covered by the array and by the higher quality of shower reconstruction, since individual showers will typically be stereoscopically imaged by a larger number of telescopes than in current few-telescope arrays. An array of 25 MSTs is foreseen for the Southern site while an array of 15 MSTs is foreseen for the Northern site. Finally for gamma energies above 10 TeV the main limitation is the small number of detected gamma-ray showers. Consequently, to achieve large improvement the array needs to cover an area of several square kilometres. At high energies the light yield of a shower is large and a small light collection as the one of the SSTs is enough to detect efficiently those high energy showers. An array of 70 SSTs is foreseen on the Southern site and will allow to cover a very large area. In Figures 4.7 the layout of the telescopes on the two sites is shown.

My research activity in CTA has been mainly focused in the last years on two aspects. In the next section I will describe the work I have done on Monte Carlo simulation of the CTA array and in particular on the simulation of one of the proposed SST telescope for CTA: the Gamma Cherenkov Telescope (GCT). In section 4.6 I will show the work in progress that have been started on the potentiality of CTA in detecting PeV galactic cosmic rays sources known as PeVatrons.

4.5 Monte Carlo simulation of GCT

Three SST telescope designs are currently proposed for CTA. One design is a one mirror Davis-Cotton [9] telescope called SST-1M that is very similar to the MST and LST design. The other two designs are dual mirror telescopes which are very innovative designs and have never been built as IACTs. One is the ASTRI (Astrofisica con Specchi a Tecnologia Replicante Italiana) project

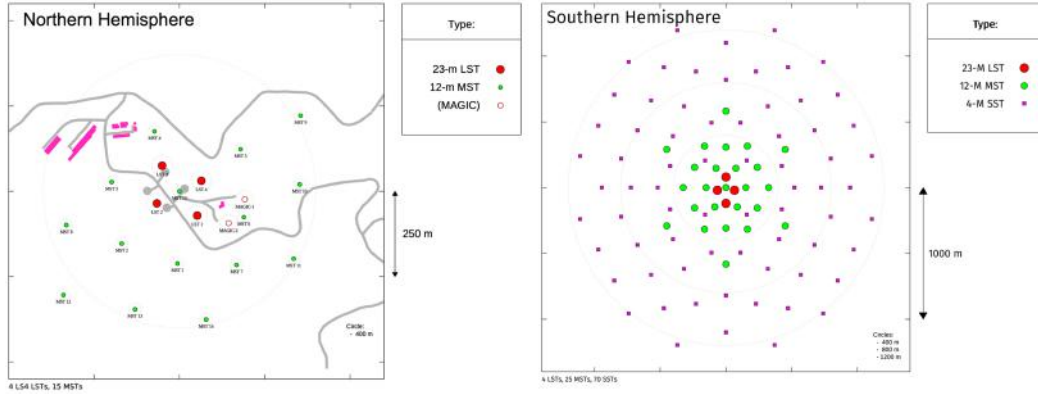


Figure 4.7: The CTA Northern Site (left): 4 LSTs and 15 MSTs (area covered by the array of telescopes: $\sim 0.6 \text{ km}^2$); The CTA Southern Site (right): 4 LSTs, 25 MSTs and 70 SSTs (area covered by the array of telescopes: $\sim 4 \text{ km}^2$).

and the other is the GCT (Gamma Cherenkov Telescope) project.

CPPM has joined GCT in 2014 and I have been responsible for the Monte Carlo simulations of this telescope until the beginning of 2018. GCT is based on a Schwarzschild-Couder [10] optical design and couples a large FoV (8°) with optimal optical performance. The primary and secondary mirrors have a diameter of 4 and 2 m respectively and Cherenkov light is focused on a compact camera based on densely-pixelated photodetectors (see Figure 4.8a).

In order to test different types of commercial available photosensors, two versions of the camera have been prototyped for GCT: one version, GCT-M, is based on Multi Anode PMTs (MaPMT) and the other, GCT-S, is based on Si PMTs. A prototype of the GCT telescope has been built at the Observatoire de Paris in Meudon and has been inaugurated with the GCT-M camera in November 2015 (see Figure 4.8a). The prototype telescope features only two out of six petals in the primary mirror (the other petals were replaced by dummies), and the primary petals are round rather than trapezoidal as planned for the final design (see Figure 4.8b).

The Monte Carlo simulation has consisted in different steps. At first we have simulated the final GCT design with the two camera versions (GCT-M and GCT-S) and obtained its performance in terms of optical efficiency, trigger efficiency and charge resolution. These figures of merit have to be obtained since each telescope design proposed to CTA have to fulfill specific requirements in order to be accepted as CTA telescope designs. We performed the simulations using the CORSIKA simulation code [11] for shower simulation in the atmosphere and the sim_telarray code [12] for detailed simulation of the



Figure 4.8: The GCT telescope. (a) is a picture of the GCT prototype built at the Observatoire de Paris in Meudon. (b) represents the final design of GCT proposed for CTA.

detection of Cherenkov light by the telescope. It should be noted that at the time at which these first simulations have been performed, the features of the final design of GCT (quantum efficiency of the photosensors, mirror reflectivity etc.) were not precisely defined. The results that are presented here are therefore preliminary and helped mainly to define some design choices such as the photosensor type (MaPMTs or SiPMTs). In particular we compared the basic performance obtained considering the two camera versions (GCT-M and GCT-S).

Optical Efficiency. It can be defined as the ratio between the photons detected by the pixel sensors and the photons directed to hit the primary mirror M1 multiplied by the area of M1. This parameter accounts for the shadowing of the different telescope components, which has been studied in a precedent work [13], for the reflectivities of both mirrors, the transmission of a protective window on the camera, the angular efficiency of the window and sensors and finally for the photon detector efficiency of the sensors. The optical efficiency has been calculated for both telescopes GCT-M and GCT-S and is wavelength and off-axis angle dependent (See Figure 4.9). It should be noticed that while GCT-S has a larger total photon detector efficiency its peak sensitivity occurs at larger wavelengths. This results in a larger Night Sky Background (NSB) rate which needs the use of dielectric mirrors or a coating on the camera window that provides a cut-off at around 550 nm at which the NSB intensity is the highest (Figure 4.9).

Charge resolution The total charge collected by the detector can be expressed as a number of photo-electrons (p.e.) and should be proportional to the Cherenkov light intensity in the pixel. The charge resolution is defined as

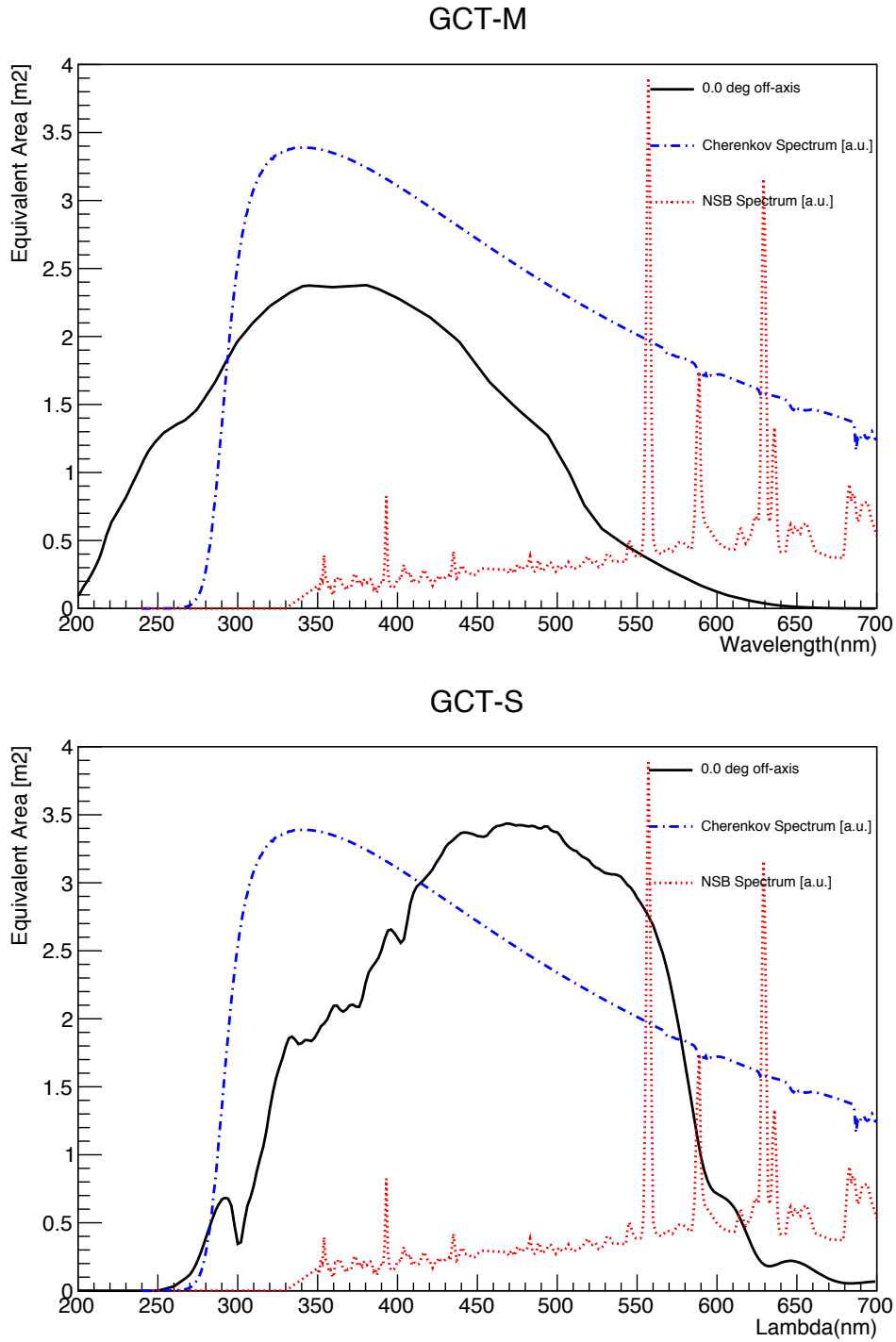


Figure 4.9: Optical efficiency of GCT-M (top) and GCT-S (bottom) as a function of the photon wavelength for on-axis photons on M1. The NSB and Cherenkov spectrum (red and blue dashed line) in arbitrary units have been placed in these figures to show the relative sensitivity ranges of GCT-M and GCT-S.

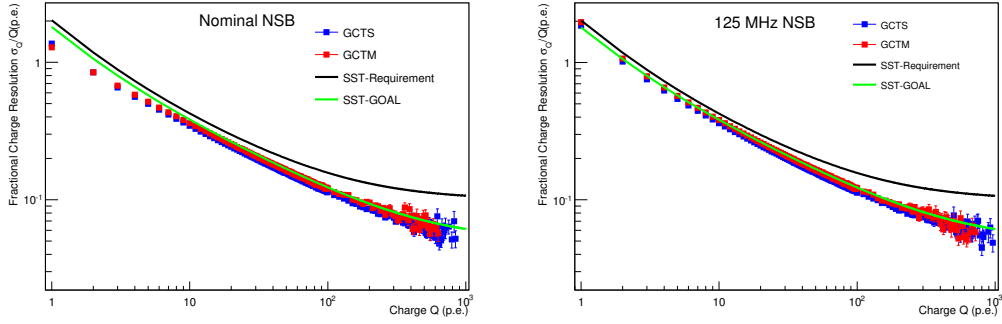


Figure 4.10: Fractional charge resolution of GCT-M (red) and GCT-S (blue) as a function of true charge in the case of low NSB scenario (left) and high NSB scenario (right).

the standard deviation of the reconstructed charge σ_Q around the simulated true charge (Q) and takes into account both the spread of the reconstructed charge distribution and the bias in respect of the simulated true charge. The acquisition system allows storage of 96 ns trace for triggered showers in each camera pixel. As the pulse FWHM is much smaller than 96 ns, to reduce the effect of the NSB photons and electronic noise, it is desirable to integrate over a shorter window around the maximum of the trace to obtain the charge of the incident photon. In the case when the Cherenkov photons and the NSB photons have similar amplitudes, the NSB contribution can prevent the correct determination of the trace maximum if one looks for the maximum of the signal in the 96 ns window. Therefore we predicted the time of the trace maximum from the time of the maximum of the weighted sum of the signals in the neighbour pixels and the specific pixel. Finally we have obtained the charge resolution for both GCT-S and GCT-M telescopes using a 12 ns integration window around the predicted time of the trace maximum. Two different NSB scenarios have been considered. The low NSB scenario corresponds to standard dark sky conditions, while the high NSB condition corresponds to the maximum NSB considered in CTA requirements (125 MHz). Figure 4.10 shows the fractional charge resolution in these two scenarios. The black and the green lines represent the requirement and goal performance required by CTA for the SSTs. As expected, in the case of high NSB the performance is worse but it is still acceptable to perform observations.

Trigger efficiency It is defined as the ratio between the number of photons that trigger the camera divided by the number of photons arriving to the camera. The trigger logic of the camera is based on a combination of 4 neighbouring pixels being required to exceed the trigger threshold. We simu-

lated 2×10^5 gamma-ray showers in the energy range 0.315 to 600 TeV out to a distance of 1200 m from a single GCT telescope. Figure 4.11 c) shows that 50 % trigger efficiency is obtained for both GCT-M and GCT-S for an image charge on the camera below 80 p.e. which is the requirement for CTA. Figure 4.11 a) and 4.11 b) show the trigger efficiency as a function of both energy and impact distance; the latter confirms the idea that SSTs can be used at larger spacing than the Cherenkov light pool (~ 120 m) to improve the chance of triggering on these showers.

The conclusion of this preliminary study was that in principle both type of sensors could be used for GCT (MaPMT and SiPMT) since in both cases CTA requirements were met[14]. However the detection efficiency of GCT-S is higher thanks to the higher sensor efficiency. Moreover at present the price of SiPMT has decreased and the experience gained in the last 2 years with the GCT-M prototype has demonstrated some problems with the operation of MaPMTs such as a very large cross-talk between pixels. The choice has been therefore to go for a SiPMT camera as final design for GCT.

In order to study the potentiality of the GCT prototype installed at Meudon, we performed a detailed simulation of the prototype to determine its sensitivity in detecting the Crab nebula [15]. For this study we considered the case in which all six petals were installed on the structure. The Crab is a standard candle for gamma-ray astronomy and is used as a calibration source for gamma-ray telescopes due to its intense flux. To this end gamma and proton showers have been simulated at the Meudon site and the event directions have been reconstructed using a mono-reconstruction [16, 17]. The Crab has been simulated as a point source at the center of the FoV of the telescope and the protons, that constitute the background for the gamma observation, have been simulated isotropically on the entire telescope field of view. For gamma-proton separation a Multi Layer Perceptron (MLP) Neural Network developed in 2001 by Jean-Pierre Ernenwein has been adopted obtaining a very good proton rejection of the order of 98% with more than 50% efficiency in gamma detection. For the gamma-ray source search a cut on the MLP variable and on the θ^2 (squared distance between the shower reconstructed position from the Mono Reconstruction and the pointed source, here at the center of the camera) has been applied. The aim of this work has been to determine the time needed to observe the Crab nebula with a 5σ significance. To this end two methods have been adopted. In a first rather conservative method the background has been estimated considering an OFF-source observation of the same duration as the ON-source observation. The final cuts have been chosen to minimize the observation time for a 5σ significance observation of the Crab nebula. The required time for a 5σ observation is 24 hours of ON-source observation

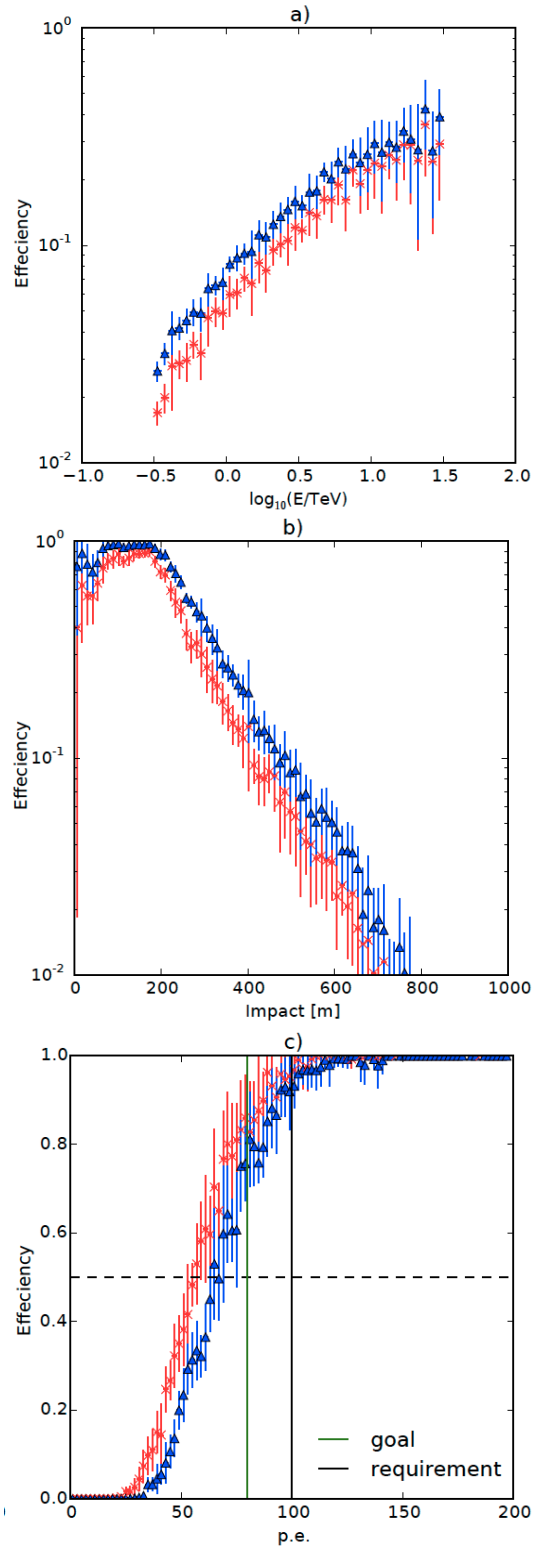


Figure 4.11: Trigger efficiency of gamma-rays for the two telescopes, GCT-M (red) and GCT-S (blue), as a function of a) Energy, b) Impact distance and c) photo-electrons

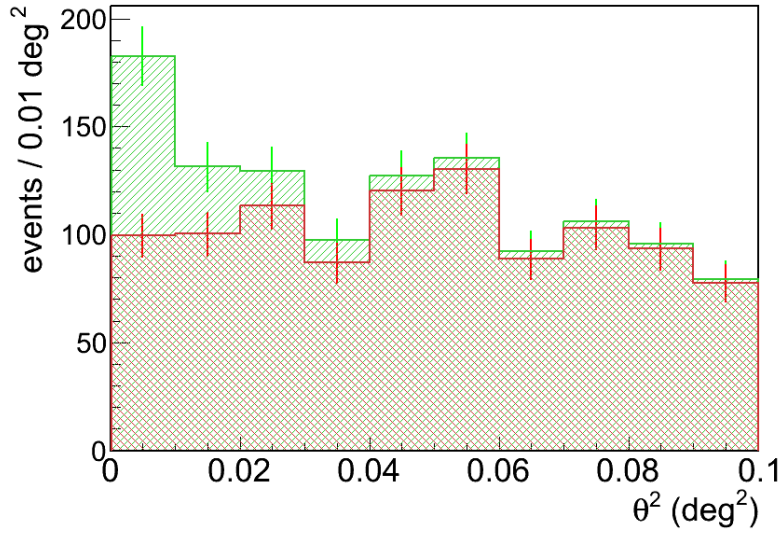


Figure 4.12: θ^2 distribution for gammas and protons after MLP cut in 24 hours observation. The green area corresponds to protons and gammas (ON-source observation), while the red zone corresponds to protons only (OFF-source observation).

and 24 hours of OFF-source observation. The θ^2 distribution of the detected events during the ON-source observation (green area: gammas and protons) and the OFF-source observation (red area: protons only) in 24 hours is shown in Figure 4.12. After the final cuts (MLP > 0.9 and $\theta^2 < 0.02 \text{ deg}^2$) $N_\gamma=114$ and $N_p=200$. The Signal over Background ratio S/B is 0.6.

In order to reduce the time needed to detect the Crab a second method called ring background method has been adopted. It consists in defining a ring around the central ON zone ($\theta^2 < 0.02 \text{ deg}^2$) to evaluate the proton background in the ON zone. The inner radius of the ring should be large enough to avoid gamma contamination: $\theta^2 > 0.1 \text{ deg}^2$. Taking into account the gamma-like proton acceptance decrease across the FoV, the outer radius is chosen to cumulate an effective collection area for gamma-like protons 10 times larger than the ON zone: $\theta^2 < 0.55 \text{ deg}^2$ (Figure 4.13).

After gamma-hadron separation cuts a proton rate of 1.4 p/min is obtained in the ring while the gamma rate is of 0.4 gamma/hour therefore the ring zone can be considered essentially gamma free. After 13 hours of ON-source observation, a 5σ observation significance is reached with $N_\gamma=62$, $N_p=1120/10$ and a Signal over Background ratio S/B=0.6. An important remark is that OFF data have to be taken to check the gamma-like proton acceptance obtained

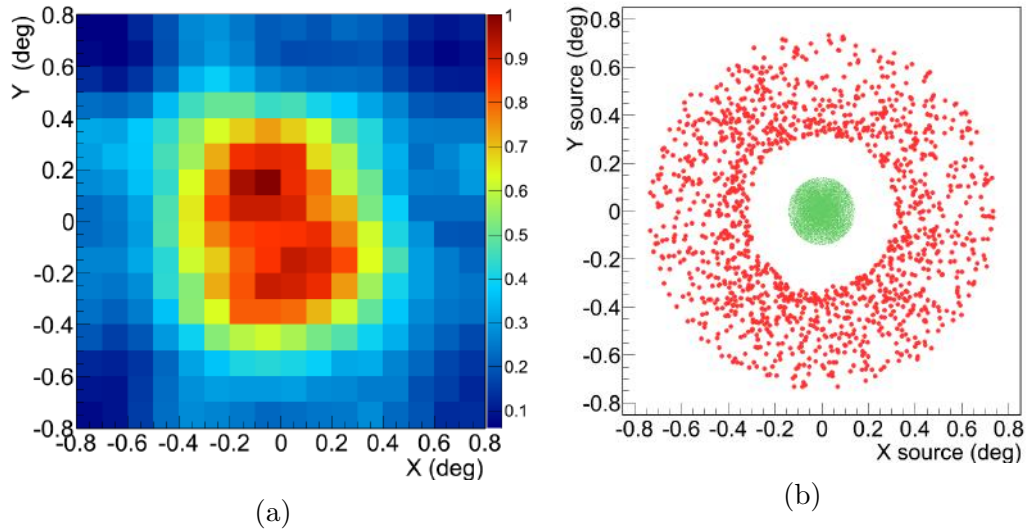


Figure 4.13: Acceptance of gamma-like protons (a). Extension of the ON (green region) and OFF zones (red region) with the events collected after cuts (b).

from simulation across the FoV. Considering a rate of 1.4 p/min inside the ring, 30 hours of pure OFF data would allow an acceptance measurement at a level of 10%.

The study has not been repeated in the case of two petals but from first order calculations it seems that the performance is decreased by at least a factor 5 meaning an increase of a factor 5 in observation time. Unfortunately due to funding problems the Meudon prototype has not been completed yet and therefore a Crab observation is not feasible with the current telescope.

A second operation campaign of the Meudon prototype has been performed in spring 2017 and data/MC comparison has been attempted for the first time. Figure 4.14 represents the comparison between data and MC of the width and length (Hillas parameters) of the reconstructed cosmic ray shower image in the camera. The MC simulation input parameters have been tuned to match the observation.

4.6 Pevatron search with CTA

One of the main science goals of CTA is to discover the origin of Galactic cosmic rays (CR). Their origin remains indeed an open question and in particular the origin of the knee in the CR spectrum around PeV energies (see Figure 3.1) is

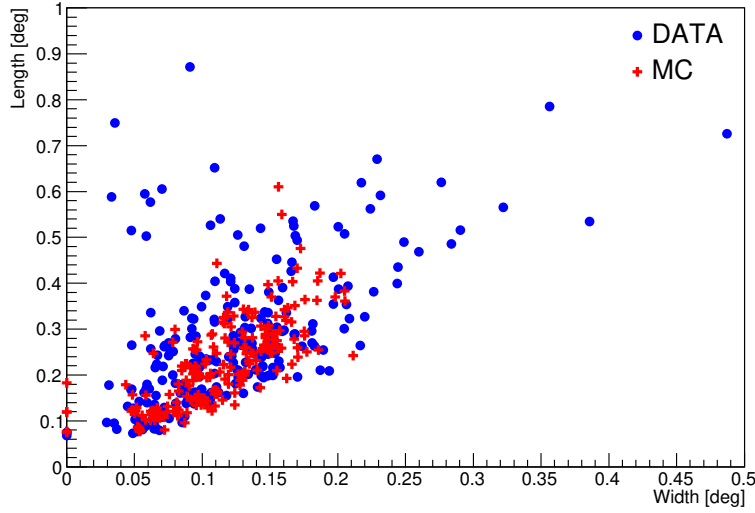


Figure 4.14: Comparison of width and length Hillas parameters between data and MC. Cosmic ray data have been taken during spring 2017 and simulations have been tuned to optimize the data-MC comparison.

still debated. It is believed that the particles with energies below the knee are accelerated by CR sources located inside the Galaxy. In order to maintain the CR intensity at the observed level, the CR sources in our Galaxy must provide 10^{41} erg/s in the form of accelerated particles. Supernova remnants (SNRs) are able to satisfy the CR energy requirement if they can convert 10% of their kinetic energy into accelerated particles via diffusive shock acceleration at the expanding SNR shocks. Due to the decay of π_0 produced in the interactions between accelerated CRs and gas swept up by the shock, SNRs should also be bright very-high-energy (VHE; $E > 0.1$ TeV) gamma-ray sources. However all observed SNRs spectra exhibit a spectral cutoff or break, significantly below 100 TeV. Furthermore since electrons can also be accelerated at SNR shocks and produce gamma-rays through inverse-Compton (IC) scattering (see section 4.1.1), current VHE observations can not resolve the problematic ambiguity between leptonic and hadronic origin in the VHE domain mostly due to low statistics at energies higher than 10 TeV. Thus, currently, it is still unclear whether or not SNRs can act as CR sources at PeV energies therefore be considered as PeVatrons. The future CTA observatory will be able to explore the VHE domain above 50 TeV (See Figure 4.6), in which the problematic ambiguity between leptonic and hadronic emission mechanisms is resolved due to the quick decrease of the IC electron-photon interaction cross-section above a few tens of TeV. The PeVatron search is a key science program of CTA consortium.

The goal is to address some of the fundamental questions of high energy CR acceleration. In particular, CTA will provide information on the distribution of PeVatrons in the Galaxy, the mechanism and effectiveness of CR acceleration at PeV energies, and determine if PeVatrons are, as currently expected, commonly associated with young SNRs. CTA will perform a complete galactic plane survey with an average flux sensitivity of 2-4 mCrab depending on Galactic coordinates with a minimum at the Galactic center. It is foreseen that the exposure time for each pointing during the GPS will be around 15 hours. During the GPS, a maximum number of 5 PeVatron candidates should be identified, for which a later deeper exposure of 50 hours will be pursued [18].

In 2016, we have started to work on the CTA PeVatron key science project. The strategy for PeVatron search proposed in the recent summary document on CTA Science goals [18] is based on the detection of a high energy spectral point at 50 TeV. This criteria does not use the information on the spectral features of the source such as the spectral index, the flux normalization and the energy cutoff in the spectrum which can be obtained by fitting the spectral data to different models. We have therefore proposed to define a selection criteria based on the spectral features of the measured source and the work has been to first estimate the observation time required for CTA to determine a potential PeVatron source. To this aim simulations of possible PeVatron sources have been performed using the package Gammapy [19] which is one of the official CTA analysis tools. For the simulations the latest Instrument Response Function for CTA have been considered and spectral data have been obtained in the case of different flux normalizations, different observation times and different intrinsic cutoff of the gamma-ray spectrum. The simulated data have then been fitted to determine a lower limit on the cutoff energy observed by CTA which we have considered as a preliminary selection criteria for determining potential PeVatron candidates [20].

We are currently investigating a larger sample of possible PeVatron candidates taking into account also different source spectral indexes besides flux normalization and intrinsic energy cut-offs. Work is also in progress for deriving the parental proton flux, in the case of hadronic gamma origin, from observed gamma-ray spectra [21]. The ultimate goal is to determine a robust and efficient selection criteria for PeVatron search during the galactic plane survey.

Bibliography

- [1] Fermi-LAT collaboration, *Astrop. J.*, 697, 1071 (2009).

- [2] H. Abdalla et al., *Astron. Astrophys.*, 612 A6 (2018).
- [3] J. Hinton and W. Hoffmann, *An. Rev.o Ast. Ast.*, 47, 523 (2009).
- [4] <http://www.hawc-observatory.org/>
- [5] A. Hillas, *Proc. ICRC (La Jolla)*, Vol 3, 445 (1985).
- [6] F. Aharonian, et al., *Astron. Astrophys.*, 457, 899 (2006).
- [7] J. Aleksic, et al., *Astropart. Phys.*, 35, 435 (2012).
- [8] J. Holder, et al., *Astropart. Phys.*, 25, 391 (2006).
- [9] J.M. Davies, E.S.J. Cotton, *Solar Energy Sci. and Eng.*, 1, 16 (1957).
- [10] V. Vassiliev et al., *Astrop. Phys.* 28, 10 (2007).
- [11] D. Heck et al.,, *Report FZKA 6019* (1998).
- [12] K. Bernlohr, *Astropart. Phys.* 30, 149 (2008).
- [13] C. Rulten, *PhD thesis, Durham University* (2012).
- [14] T. Armstrong, H. Costantini et al., *Proceedings of ICRC 2015*
- [15] H. Costantini et al., *Proceedings Gamma2016* (2016).
- [16] R.W Lessard et al, *Astrop. Phys.* 15, 1-18 (2001).
- [17] C. Bigongiari et al, *ICRC2013*, arxiv1307.5006 (2013).
- [18] CTA consortium, *arXiv:1709.07997* (2017).
- [19] <http://gammapy.org/>
- [20] C. Trichard et al., *PoS(ICRC2017)* (arXiv:1709.01311) (2017).
- [21] E.A. Angüner et al., *in preparation*

Chapter 5

Summary and perspectives

The work presented in this thesis brings together two relatively new disciplines that have developed consistently in the last decades: nuclear and particle astrophysics. In both fields the knowledge coming from the investigation of subatomic processes and the related experimental techniques is used to understand the physics of celestial objects and to answer some of the most intriguing questions in modern astrophysics, such as: which is the origin of the nuclear elements in the Universe, how does a massive star explode, which are the sources that accelerate cosmic rays detected on Earth. Nuclear reaction rates are fundamental ingredients for stellar evolutionary codes that model star evolution both in quiescent and explosive phases. In the first chapter I have presented the research I have been involved since my PhD thesis that concerns the measurement of nuclear reaction cross section occurring in different evolutionary phases of a star. In particular in the present document I focused on the precise measurement of the ${}^3\text{He}+{}^4\text{He}$ reaction which is a fundamental nuclear process of the Hydrogen burning phase in stars and directly influences the thermonuclear neutrino production. Solar neutrino fluxes have been now precisely measured at Earth [1] and allow to accurately determine the physical parameters of the Sun such as the temperature and the metallicity provided that nuclear reaction cross sections are known with similar accuracy. Neutrinos are not only produced in nuclear reactions during the quiescent life of a star but can be produced during a Supernova explosion as demonstrated by the neutrinos detected in 1987 coming from a Supernova explosion in the Large Magellanic Cloud (SN1987A). Finally neutrinos are also supposed to be produced in the surroundings of high energetic sources such as the remnants of supenova explosions or in the jets produced close to extreme sources such as massive and supermassive black holes. According to astrophysical models neutrinos are produced by energetic cosmic rays accelerated in high energy sources, interacting with material and radiation fields in the source environment. The

detection of a high energy neutrinos from an astrophysical source would therefore represent a major discovery since it would prove the existence of cosmic ray production in the source. The research I present in the second chapter is indeed linked to the ANTARES neutrino detector that has been built with the main goal to measure high energy astrophysical neutrinos coming from high energetic sources. My work in ANTARES has been mainly focused on the calibration and simulation of the detector and I have used those expertises to study the possibility to detect with ANTARES low energy neutrinos coming from a galactic supernova explosion. High energy neutrinos have been now measured as a diffused flux by the IceCube detector, which is a factor 10 bigger than ANTARES, but a clear high energy neutrino signal from an astrophysical source is still missing. Nevertheless the diffused astrophysical neutrino flux measured by IceCube has been a main breakthrough in particle astrophysics and brings hope in the exploitation of high energy neutrinos to investigate the high energy universe.

Charged particles accelerated in astrophysical sources can interact with matter and radiation fields producing also high energy gamma radiation that can be efficiently measured on Earth by means of ground based gamma detectors. High-energy gamma-ray observations have produced indeed in the last decade a lot of exciting results. CTA is a new instrument based on the actual detectors technology, which should become operational in the next years and will improve the detection sensitivity by an order of magnitude. In chapter 3 I present the research field of gamma astrophysics and the preparation work for CTA that is presently undergoing at CPPM. My work has been mainly related to Monte Carlo simulation of the CTA telescopes aimed to define the performance and optimize the design. CTA has several scientific goals, but for sure one of the most exiting goal will be the search for galactic cosmic rays. CTA will in fact explore for the first time the very high energy region above few tens of TeV. At those extreme energies gammas are mainly produced by cosmic rays and a detection of sources emitting gammas at those energies would clearly identify a cosmic ray source as a neutrino signal would do. As mentioned at the end of chapter 3 the CTA-CPPM group is since two years leading the PeVatron working group for CTA. PeVatrons are the sources that are expected to emit cosmic rays at PeV energies. We have been working on the estimation of the sensitivity of CTA in detecting PeVatron sources in our Galaxy with the main goal to define a reliable and robust criteria to identify possible PeVatron sources during the Galactic Plane Survey that will be a major observation effort for CTA. During the survey, which will be performed by CTA with a factor ten higher sensitivity in respect to present surveys, it is expected that new sources will be discovered. From these first observations

CTA will choose a limited number of sources for which a deeper observation will be performed. It is therefore crucial to define the best criteria possible to make the best choice of potential PeVatron candidates.

The discovery of cosmic ray sources both in and outside our Galaxy could also come from direct detection of neutrinos. A very promising strategy is to combine measurements from gamma rays and neutrinos in order to enhance the discovery potential. A coincident detection of high energy neutrino from IceCube and high energy gammas detected by the MAGIC Cherenkov telescope and the Fermi satellite has been announced very recently [2, 3]. This is the first evidence of a high energy neutrino signal from a source which has been identified as a distant blazar already observed in the past. With CTA and the next generation neutrino telescopes as KM3NeT getting in operation, the possibility of coincident detection between high energy neutrinos and gammas will become larger allowing to detect cosmic ray sources and to study in details the mechanisms of CR production in the Universe. The last two years have been also extremely exciting for astroparticle physics thanks to the discovery of gravitational waves from merging black holes and neutron stars [4, 5]. In particular in summer 2017 a coincident detection of gravitational waves from two merging neutron stars and photons from all wavebands (from radio to gammas) has allowed to study in impressive details a kilonova source bringing a large amount of information on this specific source. Observations of photons and gravitational waves from a single source has allowed to shed first light on a lot of fundamental questions in astrophysics such as the nature of progenitors of a kilonova, the origin of short gamma-ray bursts, the origin of heavy elements in the universe and many others. We are now entered in the era of multimessenger astronomy where not only photons but also neutrinos, gravitational waves and eventually cosmic rays are used to explore the Universe.

In this context the perspective in the next years is to continue the work that I have started since few years in CTA. On a technical point of view the plan is to finalize the contribution to the construction of the instrument with the goal to exploit the data coming from the first telescopes. In the last years I have gained experience with Monte Carlo simulation first of the GCT telescope, which is one of the proposed SST telescopes for CTA and very recently with the simulation of the MST telescope and in particular of the NectarCAM camera which is the main french contribution to CTA. The final goal is to have a reliable MC model for the entire CTA and first data/Monte Carlo comparisons with prototype data have been started. A precise Monte Carlo simulation of CTA is fundamental to achieve the challenging performance that CTA aims for.

On the scientific point of view I plan to continue the effort on the definition

of the criteria for PeVatron search with CTA and I plan to study the CTA potentiality in studying the nature of specific sources that have been identified as promising PeVatron candidates by present instruments such as H.E.S.S..

Finally I would like to exploit the expertise in astrophysical neutrino detection I gained with ANTARES and the opportunity to have both gamma and neutrino astrophysics at CPPM. In particular the goal is to reinforce the multimessenger aspect in our lab working first on common perspectives in the search for cosmic ray sources both with CTA and KM3NeT and once the instruments will start to produce data, perform joint analysis in order to enhance the chance of discoveries.

Bibliography

- [1] Borexino Collaboration, *Nature*, volume 562, pages 505510 (2018).
- [2] IceCube Collaboration, *Science*, volume 361, issue 6398, pages 147-151 (2018).
- [3] MAGIC Collaboration, *The Astrophysical Journal Letters*, volume L10, 863 (2018).
- [4] LIGO and Virgo Collaboration, *Phys. Rev. Lett.* volume 116, 061102 (2016).
- [5] LIGO and Virgo Collaboration, *Phys. Rev. Lett.* volume 119, 161101 (2017).

Appendix A

Curriculum Vitae

Curriculum Vitae
of
Heide Costantini
12 April 2019

Personal information

Name Heide
Surname Costantini
Birth Perugia (Italy), May 14, 1975
Nationality Italian and German
Civil Status Married
Work address Centre de Physique des Particules de Marseille (CPPM)
Aix-Marseille Université 163,
Av.de Luminy, case 902, 13288 Marseille Cedex 09
phone +33 0491 827257 **fax** +33 0491 827299
email costantini@cppm.in2p3.fr

Formation

Jun.'03 PhD in Physics, Università di Genova, Genoa, Italy.
Thesis: “Direct measurement of radiative capture reactions at astrophysical energies”.

Sep.'99 Five Years Degree in Physics (*Laurea in Fisica*), Università di Genova, Genoa, Italy.
Thesis: “Measurement of the electron screening for the $^3\text{He}+d$ reaction at astrophysical energies”.

Jun.'94 High school diploma, Liceo Scientifico “Vittorio Sereni,” Luino (VA), Italy.

Work experiences

- Oct.'10 – Present** Assistant Professor (*Maître de conférences*) at Aix-Marseille Université, France.
- Oct.'06 – Sep. '10** Staff Researcher at INFN (Istituto Nazionale Fisica Nucleare), Genoa, Italy.
- Oct.'05 - Oct.'06** Post-Doc Research Associate at NSL (Nuclear Structure Laboratory), Notre Dame University, IN, USA.
- Aug.'03 - Aug.'05** INFN Fellow Researcher at the Department of Physics, Università di Genova, Genoa, Italy.

Achievements and Responsibilities

- Jan '19- present** Nominated member of the Scientific Council of IN2P3-CNRS
- Sep '18- present** Member of Project Committee of NectarCAM (project of a camera for Medium Sized Telescopes for CTA)
- May '17- present** CTA group-leader at CPPM (Centre de Physique des Particules de Marseille)
- May '17- present** Responsible of organization of TIPE (Travaux d'Initiative Personelle Encadres) fof CPPM (Centre de Physique des Particules de Marseille)
- Dec. '16- present** Elected member of the Scientific Council of the CPPM (Centre de Physique des Particules de Marseille)
- 2015-2016** Responsible for seminar organization of CPPM (Centre de Physique des Particules de Marseille)
- Dec. '09- Dec. '15** Member of the International Advisory Committee of “ JINA reaclib” database for astrophysical reaction rates

- Oct.'08 – Jun.'14** Member of the steering committee as calibration coordinator of the ANTARES (Astronomy with a Neutrino Telescope and Abyss environmental RESearch) experiment
- Sep.'11 - Sep.'12** Responsible of the first year License “Physique et Chemie” at Aix-Marseille Université, France.
- Feb.'07** Qualification as Assistant Professor (*Maître de conférences*) for Elementary constituents (*Section 29 - Constituants élémentaires*) and Astronomy and Astrophysics (*Section 34 - Astronomie, astrophysique*) released by the French Ministry of Education and Research.
- A.Y.'97-'99** Student Delegate of the Department Committee at the Department of Physics at the Università di Genova

Scientific activities

- 2010 - current** *participation to the CTA consortium for the construction of a Cherenkov Telescope Array for gamma ray astronomy*
- studies and first tests for the construction of a new type of light collector for Small Size Telescopes (SST)
 - Evaluation of site candidates for hosting CTA
 - study of telescopes performance using Monte Carlo simulations
 - coordinator of the Monte Carlo working group of GCT sub consortium for the construction of dual mirrors SSTs for CTA (2014-2017)
 - study of CTA performance in detecting cosmic rays Accelerators (PeVatrons)
 - member of the MC-Validation task-force for CTA Observatory
 - coordinator of the Monte Carlo working group of NectarCAM project for the construction of a camera for MSTs for CTA
- 2007 - 2017** *participation to the ANTARES experiment for the detection of astrophysical neutrinos in the Mediterranean Sea*
- coordinator of the calibration working group (25 people) (2008-2014)
 - feasibility study for the detection of low energy supernova Neutrinos
 - analysis of the detection of neutrinos coming from the « Fermi Bubbles »
 - measurement of the ANTARES Optical Module (OM) angular acceptance and detection efficiency
 - development of a Monte Carlo code to describe the OM features

1998 – 2010 *participation to the LUNA experiment for the measurement of nuclear reaction of astrophysical interest at the Gran Sasso National Underground Laboratory*

- member of the working group for the measurement of the $^{17}\text{O}(p,\gamma)^{18}\text{F}$ (hydrogen burning in massive and AGB stars and fluorine synthesis in nova outbursts)
- member of the working group for the measurement of the $\text{D}(\alpha,\gamma)^6\text{Li}$, (key reaction for ^6Li production in Big Bang nucleosynthesis)
- member of the working group for the redaction of the proposal for a 3 MV accelerator at the Gran Sasso National Laboratory
- measurement of the $^{15}\text{N}(p,\gamma)^{16}\text{O}$ (CNO cycle of Hydrogen burning)
- measurement of the $^3\text{He}(\alpha,\gamma)^7\text{Be}$ (^8B and ^7Be solar neutrino flux)
- measurement of the $^{14}\text{N}(p,\gamma)^{15}\text{O}$ (CNO solar neutrino flux and age globular clusters)
- measurement of $\text{D}(p,\gamma)^3\text{He}$ (Big-Bang nucleosynthesis)
- measurement of $^3\text{He}(d,p)^4\text{He}$ (electron screening effect)

Oct'05-Oct.'06 *participation to JINA (Joint Institute for Nuclear Astrophysics) at the University of Notre Dame*

- measurement of the $^{16}\text{O}(\alpha,\gamma)^{20}\text{Ne}$ reaction (He-burning and later evolutionary phases in massive stars)
- development of an R-matrix code (AZURE) for extrapolation of reaction cross section at astrophysical energies

Summary of personal scientific production

- ~100 papers in peer-reviewed international journals
- 18 proceedings of international conferences
- 12 invited talks and 9 contributed talks at international conferences
- 4 posters presented at international conferences
- 18 invited seminars
- 2 invited lectures at international schools

Reviewing

Astroparticle Physics, Proceedings of 9th Symposium on Nuclei in the Cosmos, Nuclear Physics A, European Physical Journal A

Grants

2015-2019 CPPM team project leader of the Labex-OCEVU grant for the project “ *Preparing OCEVU's CTA Science (CTASci)*” (2 postdoc positions for 3 years+20 keuro operating budget)

- 2011** PI of the grant BQR project "*Étude et réalisation d'un prototype de collecteur de lumière pour la caméra des télescopes gamma dans le cadre du projet CTA*" of the Université de la Méditerranée (Marseille) (28 keuro)

Event Organization

- Jul. '17** Member of the Organising Committee of the "*Ecole d'été Franco-Chinoise*" for M1 Physics students from Chinese universities, CPPM, Marseille, France
- May '15** Member of the Organising Committee of the "*OCEVU Summer Camp*" for second year Physics students of Montpellier, Toulouse and Aix-Marseille universities, CPPM, Marseille, France
- Feb. '13** Member of the international organising committee of the Workshop "*Starting-up the LUNA MV collaboration*" Gran Sasso Laboratory, Italy.
- Sep. '12** Organizer of the conference "*Toward a probabilistic representation of the world*", Luino, Italy.
- Jan. '09** Member of the international organizing committee of the Workshop "Solar Fusion II", January 2009 Seattle, WA, USA.
- June '09** Organizer of the ANTARES Collaboration meeting, June 2009 Genova, Italy.

Consulting

Invited scientific consultant for DIANA (Dakota Ion Accelerator in Nuclear Astrophysics) project submitted to NSF (National Science Foundation) for the installation of an accelerator in the new underground DUSEL (Deep Underground Science and Engineering Laboratory), SD, USA.

Teaching

- July '18** Lecturer at 2018 French-Chinese Summer School "*Physics for both infinities*" for M1 Chinese Physics students CPPM, Marseille, France
- July '17** Lecturer at 2017 French-Chinese Summer School "*Physics for both infinities*" for M1 Chinese Physics students CPPM, Marseille, France
- May '15** Lecturer at "*OCEVU Summer Camp*" for second year Physics students of Montpellier, Toulouse and Aix-Marseille universities, CPPM, Marseille, France
- A.Y.'18-'19** M1 class of Statistics and Data analysis, Aix-Marseille Université, Marseille, France
- A.Y.'18-'19** Second year Physics class for the *Licence de Physique*, Aix-Marseille Université, Marseille, France
- A.Y.'16-'17-present** First year Physics class for the *Licence de Physique*, Aix-Marseille Université, Marseille, France
- A.Y.'10-'11-present** First year Physics class for the *Licence de Sciences de la Mer et de l'Environnement*, Aix-Marseille Université, Marseille, France
- A.Y. '12-'13, '13-'14** Lectures on "Gamma astrophysics" at the Astroparticle class for last year Master students, Aix-Marseille Université, Marseille, France
- Feb. '10** Invited lecturer at 13th International Moscow School of Physics (38th ITEP Winter School of Physics), Moscow, Russia
- A.Y.'07-'08** Teaching Assistant, 4th year course "Radioactivity", Faculty of Science, Università di Genova, Genoa, Italy.
- A.Y.'06-'07** Teaching Assistant, 4th year course "Radioactivity", Faculty of Science, Università di Genova, Genoa, Italy.
- Oct.'05** Invited Lecturer at "3rd European Summer School on Experimental Nuclear Astrophysics", S.Tecla, Catania, Italy.
- A.Y.'03-'04** Teaching Assistant, 4th year course "Radioactivity", Faculty of Science, Università di Genova, Genoa, Italy.
- A.Y.'01-'02** Teaching Assistant, 1th year course "Fundamentals of Physics", Faculty of Engineering, Università di Genova, Genoa, Italy.
- A.Y.'01-'02** Student Tutor at the Department of Physics, University of Genova, Genoa, Italy.

Mentoring

- 2018-2021** Co-advisor of the PhD thesis of Gaia Verna "*CTA potentiality in detecting galactic PeVatrons*" Aix-Marseille University,
- 2018** Advisor of the M2 stage of Gaia Verna "*CTA potentiality in detecting galactic PeVatrons*", student of Università degli Studi di Genova (Italy)
- 2017-2018** Co-advisor for the first year PhD thesis of Anton Dmytriiev "*CTA potentiality in the detection of Active Galactic Nuclei at extreme energies*" Paris 7 University
- Feb.'18-present** Responsible of Labex-OCEVU post-doc grant of Ekrem Oguzhan Angüner for the project "*Preparing OCEVU's CTA Science (CTASci)*"
- 2017** Advisor of the M1 stage of Julien Lucas "*Comparaison entre données expérimentales et simulation Monte Carlo pour le prototype GCT (Gamma Cherenkov Telescope) de l'observatoire d'astronomie gamma CTA*", student of Aix-Marseille Université
- 2016** Advisor of the M1 stage of Clement Bordereau "*Evaluation du potentiel de CTA pour la recherche d'accélérateurs de rayons cosmiques*", student of Aix-Marseille Université
- Oct. '15-Oct. '17** Responsible of Labex-OCEVU post-doc grant of Cyril Trichard for the project "*Preparing OCEVU's CTA Science (CTASci)*"
- Sep. '15** Member of PhD thesis jury of Cyril Trichard (Université de Grenoble)
- 2015** Advisor of the M1 stage of Guillaume Dumas "*Etude par simulations de télescopes imageurs de gerbes atmosphériques*", student de Université Paris Sud.
- 2014** Advisor of the M1 stage of Edouard Foulon "*Simulation de la detection de gammas par des telescopes imageurs de cascades atmospheriques par effet Tcherenkov. Projet CTA.*", étudiante de Aix-Marseille Université.
- 2013** Co-Advisor of the M1 stage of Julie KHAYADJIAN "*Etude par simulations de télescopes imageurs de gerbes atmosphériques*", étudiante de Aix-Marseille Université
- 2010-2013** Co-advisor of the PhD thesis of Vladimir Kulikovskiy "*Neutrino astrophysics with the ANTARES telescope*", Università degli studi di Genova, Genoa, Italy.
- 2012** Advisor of the L3 stage of Anaïs Abramian, étudiante de l'Ecole National Superior de Lyon
- Oct. 2010** Member of PhD thesis jury of Francisco Salesa (University of Valencia, Spain)

A.Y.'07-'08

Advisor of the *Laurea* Thesis in Physics of Luca Agostino “*Feasibility study for an underground measurement of the $D(\alpha,\gamma)^6\text{Li}$ reaction cross section*” Università degli Studi di Genova, Genoa, Italy.